



Defense Threat Reduction Agency
8725 John J. Kingman Road, MS
6201 Fort Belvoir, VA 22060-6201



DTRA-TR-15-45

TECHNICAL REPORT

Exploiting Novel Radiation-Induced Electromagnetic Material Changes for Remote Detection and Monitoring: Final Progress Report

Distribution Statement A. Approved for public release; distribution is unlimited.

April 2016

IACRO 09-4692I

John S. McCloy et al.

Prepared by:
Pacific Northwest National
Laboratory
902 Battelle Boulevard
Richland, WA 99352

DESTRUCTION NOTICE:

Destroy this report when it is no longer needed.
Do not return to sender.

PLEASE NOTIFY THE DEFENSE THREAT REDUCTION
AGENCY, ATTN: DTRIAC/ J9STT, 8725 JOHN J. KINGMAN ROAD,
MS-6201, FT BELVOIR, VA 22060-6201, IF YOUR ADDRESS
IS INCORRECT, IF YOU WISH IT DELETED FROM THE
DISTRIBUTION LIST, OR IF THE ADDRESSEE IS NO
LONGER EMPLOYED BY YOUR ORGANIZATION.

REPORT DOCUMENTATION PAGE

Form Approved
OMB No. 0704-0188

Public reporting burden for this collection of information is estimated to average 1 hour per response, including the time for reviewing instructions, searching existing data sources, gathering and maintaining the data needed, and completing and reviewing this collection of information. Send comments regarding this burden estimate or any other aspect of this collection of information, including suggestions for reducing this burden to Department of Defense, Washington Headquarters Services, Directorate for Information Operations and Reports (0704-0188), 1215 Jefferson Davis Highway, Suite 1204, Arlington, VA 22202-4302. Respondents should be aware that notwithstanding any other provision of law, no person shall be subject to any penalty for failing to comply with a collection of information if it does not display a currently valid OMB control number. **PLEASE DO NOT RETURN YOUR FORM TO THE ABOVE ADDRESS.**

1. REPORT DATE (DD-MM-YYYY)		2. REPORT TYPE		3. DATES COVERED (From - To)	
4. TITLE AND SUBTITLE				5a. CONTRACT NUMBER	
				5b. GRANT NUMBER	
				5c. PROGRAM ELEMENT NUMBER	
6. AUTHOR(S)				5d. PROJECT NUMBER	
				5e. TASK NUMBER	
				5f. WORK UNIT NUMBER	
7. PERFORMING ORGANIZATION NAME(S) AND ADDRESS(ES)				8. PERFORMING ORGANIZATION REPORT NUMBER	
9. SPONSORING / MONITORING AGENCY NAME(S) AND ADDRESS(ES)				10. SPONSOR/MONITOR'S ACRONYM(S)	
				11. SPONSOR/MONITOR'S REPORT NUMBER(S)	
12. DISTRIBUTION / AVAILABILITY STATEMENT					
13. SUPPLEMENTARY NOTES					
14. ABSTRACT					
15. SUBJECT TERMS					
16. SECURITY CLASSIFICATION OF:		17. LIMITATION OF ABSTRACT	18. NUMBER OF PAGES	19a. NAME OF RESPONSIBLE PERSON	
a. REPORT	b. ABSTRACT			c. THIS PAGE	19b. TELEPHONE NUMBER (include area code)

UNIT CONVERSION TABLE
U.S. customary units to and from international units of measurement*

U.S. Customary Units	Multiply by ← Divide by [†]	International Units
Length/Area/Volume		
inch (in)	2.54 $\times 10^{-2}$	meter (m)
foot (ft)	3.048 $\times 10^{-1}$	meter (m)
yard (yd)	9.144 $\times 10^{-1}$	meter (m)
mile (mi, international)	1.609 344 $\times 10^3$	meter (m)
mile (nmi, nautical, U.S.)	1.852 $\times 10^3$	meter (m)
barn (b)	1 $\times 10^{-28}$	square meter (m^2)
gallon (gal, U.S. liquid)	3.785 412 $\times 10^{-3}$	cubic meter (m^3)
cubic foot (ft^3)	2.831 685 $\times 10^{-2}$	cubic meter (m^3)
Mass/Density		
pound (lb)	4.535 924 $\times 10^{-1}$	kilogram (kg)
unified atomic mass unit (amu)	1.660 539 $\times 10^{-27}$	kilogram (kg)
pound-mass per cubic foot ($lb\ ft^{-3}$)	1.601 846 $\times 10^1$	kilogram per cubic meter ($kg\ m^{-3}$)
pound-force (lbf avoirdupois)	4.448 222	newton (N)
Energy/Work/Power		
electron volt (eV)	1.602 177 $\times 10^{-19}$	joule (J)
erg	1 $\times 10^{-7}$	joule (J)
kiloton (kt) (TNT equivalent)	4.184 $\times 10^{12}$	joule (J)
British thermal unit (Btu) (thermochemical)	1.054 350 $\times 10^3$	joule (J)
foot-pound-force (ft lbf)	1.355 818	joule (J)
calorie (cal) (thermochemical)	4.184	joule (J)
Pressure		
atmosphere (atm)	1.013 250 $\times 10^5$	pascal (Pa)
pound force per square inch (psi)	6.984 757 $\times 10^3$	pascal (Pa)
Temperature		
degree Fahrenheit ($^{\circ}$ F)	$[T(^{\circ}F) - 32]/1.8$	degree Celsius ($^{\circ}$ C)
degree Fahrenheit ($^{\circ}$ F)	$[T(^{\circ}F) + 459.67]/1.8$	kelvin (K)
Radiation		
curie (Ci) [activity of radionuclides]	3.7 $\times 10^{10}$	per second (s^{-1}) [becquerel (Bq)]
roentgen (R) [air exposure]	2.579 760 $\times 10^{-4}$	coulomb per kilogram ($C\ kg^{-1}$)
rad [absorbed dose]	1 $\times 10^{-2}$	joule per kilogram ($J\ kg^{-1}$) [gray (Gy)]
rem [equivalent and effective dose]	1 $\times 10^{-2}$	joule per kilogram ($J\ kg^{-1}$) [sievert (Sv)]

* Specific details regarding the implementation of SI units may be viewed at <http://www.bipm.org/en/si/>.

[†]Multiply the U.S. customary unit by the factor to get the international unit. Divide the international unit by the factor to get the U.S. customary unit.

DISCLAIMER

This report was prepared as an account of work sponsored by an agency of the United States Government. Neither the United States Government nor any agency thereof, nor Battelle Memorial Institute, nor any of their employees, makes **any warranty, express or implied, or assumes any legal liability or responsibility for the accuracy, completeness, or usefulness of any information, apparatus, product, or process disclosed, or represents that its use would not infringe privately owned rights.** Reference herein to any specific commercial product, process, or service by trade name, trademark, manufacturer, or otherwise does not necessarily constitute or imply its endorsement, recommendation, or favoring by the United States Government or any agency thereof, or Battelle Memorial Institute. The views and opinions of authors expressed herein do not necessarily state or reflect those of the United States Government or any agency thereof.

PACIFIC NORTHWEST NATIONAL LABORATORY
operated by
BATTELLE
for the
UNITED STATES DEPARTMENT OF ENERGY
under Contract DE-AC05-76RL01830

Printed in the United States of America

**Available to DOE and DOE contractors from the
Office of Scientific and Technical Information,
P.O. Box 62, Oak Ridge, TN 37831-0062;
ph: (865) 576-8401
fax: (865) 576-5728
email: reports@adonis.osti.gov**

**Available to the public from the National Technical Information Service,
U.S. Department of Commerce, 5285 Port Royal Rd., Springfield, VA 22161
ph: (800) 553-6847
fax: (703) 605-6900
email: orders@ntis.fedworld.gov
online ordering: <http://www.ntis.gov/ordering.htm>**



This document was printed on recycled paper.

(9/2003)

TABLE OF CONTENTS

1	Executive Summary.....	8
2	Technical approach.....	11
2.1	Detection concept.....	11
2.2	Radiation sensitive materials.....	13
2.3	Preliminary material selection.....	15
2.4	Potential applications	16
2.5	Specific approach to this project	16
3	Technical highlights	17
3.1	Detector materials	17
3.1.1	As _x Si _{1-x} semiconducting glasses	18
3.1.2	BaFe ₁₂ O ₁₉ magnets.....	19
3.1.3	Granular Iron oxide films.....	20
3.1.4	Cd _{1-x} Mn _x Te	21
3.1.5	The photomagnetic effect (PME).....	21
3.1.6	Ni,Co:CuMn ₂ O ₄ spin cluster glasses	24
3.1.7	Y ₃ Fe ₅ O ₁₂ and rare earth garnets.....	25
3.1.8	Magnetic chalcogenide spinels	26
3.1.9	Ferroelectrics.....	30
3.1.10	Mica	30
3.2	Resonators	31
3.2.1	Electromagnetic modeling of resonators and materials	31
3.2.1.1	Model Validation using Dielectric-Loaded Cylindrical Resonator	32
3.2.1.2	Model Validation using Dielectric-Loaded Rectangular Resonator.....	33
3.2.1.3	Resonator Bore Shape	34
3.2.1.4	Feed Loop Location	35
3.2.1.5	Resonator with Integrated Radiating Element.....	35
3.2.1.6	Magnetic-Loaded Split-Ring Resonator	38
3.2.1.7	Dielectric-Loaded Split-Ring Resonator	39
3.2.1.8	Summary.....	40
3.2.2	Static resonant cavity measurements	41
3.2.3	Design, construction, and testing of GEN-1 feedback amplifier	43
3.2.3.1	Resonator Feedback Loop	46
3.2.3.2	Downconversion and Display.....	46
3.2.3.3	Radiation testing of GEN-1 feedback amplifier	47
3.2.4	Design, construction, and testing of GEN-2 feedback amplifier	49
3.2.4.1	Split ring resonators (SRRs)	50
3.2.4.2	Radiation testing of GEN-2 feedback amplifier and SRR	52
4	Conclusions on device feasibility and proposed future work.....	56

5	Programmatic accomplishments.....	59
5.1	Education, collaborations, and team acknowledgements.....	59
5.1.1	PNNL team	59
5.1.2	Tufts team	59
5.1.3	Collaborations.....	59
5.2	Technical products.....	60
5.2.1	Publications.....	60
5.2.2	Patents	61
5.2.3	Presentations	61
6	References	63

TABLE OF FIGURES

Figure 2-1: Concept for radiation-induced transient or permanent change in the magnetic permeability (μ) or dielectric permittivity (ϵ)	12
Figure 2-2: One possible concept of operations for the radiation detector	12
Figure 3-1: Bulk BaFe ₁₂ O ₁₉ commercial ceramic magnets (McMaster Carr) backwards wave oscillator transmittance and reflectance measurements in the (a, left) Q band (33-50 GHz) and V band (50-70 GHz) and the (b, right) W band (75-110 GHz).	20
Figure 3-2: Permeability as a function of time showing disaccommodation processes (from Ref (Metselaar and Huyberts 1974)). (a) photo-induced effect of class II at two different temperatures; (b) thermally induced disaccommodation; (c) photo-induced disaccommodation	24
Figure 3-3: XRD spectra showing the progression of (A) CoCr ₂ S ₄ and (B) CdCr ₂ Se ₄ spinel production of repeated heat treatments.	29
Figure 3-4: AC magnetic spectrum of CoCr ₂ S ₄ showing real (χ') and imaginary (χ'') components as a function of various magnetic histories, field cooling (FC) under different fields, zero-field cooling (ZFC) then warming in different fields and from different starting states (demagnetized, remnant). The arrows show the direction of the measurement with temperature. The Curie temperature shows a sharp spike in both χ' and χ'' , particularly when the measurement is taken with no applied DC field.	29
Figure 3-5: Mica samples: phlogopite (left) and lepidolite (right)	31
Figure 3-6: HFSS model of cylindrical split-ring resonator in reference (Kelly and Gallagher 1987). (A) Eigenmode solver (B) Driven modal solver	32
Figure 3-7: Results of HFSS model of cylindrical split-ring resonator with dielectric loading. (A) Resonant frequency versus dielectric constant (B) Unloaded quality factor versus dielectric loss tangent.....	33
Figure 3-8: HFSS model of rectangular split-ring resonator in reference (Young et al. 2003). The design incorporates a dielectric shim for thermal management.	34
Figure 3-9: Example comparison of published results and HFSS predictions for rectangular split-ring resonator with dielectric loading. (A) Published data (B) HFSS predictions	34

Figure 3-10: Views of HFSS model of rectangular SRR coupled to Vivaldi antenna.	36
Figure 3-11: Results of HFSS model of rectangular SRR coupled to Vivaldi antenna. (A) Return loss (B) Electric field distribution.....	36
Figure 3-12: View of HFSS model of rectangular SRR coupled to dielectric-loaded TEM horn antenna.	37
Figure 3-13: Results of HFSS model of rectangular SRR coupled to TEM horn antenna. (A) Return loss (B) Electric field distribution.....	38
Figure 3-14: Cylindrical SRR with Barium Hexaferrite magnetic loading. (A) View of HFSS model (B) Actual resonator and inductive coil.	39
Figure 3-15: Comparison of HFSS prediction & measurement for return loss of magnetic-loaded SRR.	39
Figure 3-16: Summary of direct comparison of parametric eigenmode simulations of the same SRR loaded with ferroelectric (left column) or magnetic (right column) materials. (A) and (B) show simulations of the confinement of the electric or magnetic fields, respectively. (C) and (D) show the change in resonant frequency as a function of permittivity or permeability, respectively. (E) and (F) show the Q factors as a function of dielectric or magnetic loss tangent, respectively.	40
Figure 3-17: Resonant cavities tested. Note the two sizes of the SRR cavities (dimensions in Table VI).....	42
Figure 3-18: Schematic block diagram of regenerative amplifier circuit.....	45
Figure 3-19: Circuit implementation of regenerative amplifier. (A) Down-conversion plate (B) Resonator plate.....	45
Figure 3-20: Arrangement for irradiation testing using regenerative amplifier	46
Figure 3-21: Arrangement for irradiation testing of GEN-1 system. (Top) overall experimental set-up. (Bottom, left) Cs-137 source over split-post dielectric resonator. (Bottom, right) Cf-252 sources with polyethylene moderators over dielectric ring resonator.	48
Figure 3-22: Regenerative amplifier circuit with split post dielectric resonator on thermo-electric cooler block.....	49
Figure 3-23: SRR#1 with closed sides. The plate contains both the resonator circuit and the SRR with CdTe inside the aluminum box.	50
Figure 3-24: SRR#2 with open sides. The plate contains both the resonator circuit and the SRR. Shown are the SRR with periodically poled LiTaO ₃ in the slot and with YIG in the bore.	51
Figure 3-25: Configuration of the GEN-2 resonator for radiation testing. Si wafer is in the SPDR. The acrylic case shown at right is placed on top of the resonator, and the sources are placed on top of the case.....	52
Figure 3-26: Example output waveforms from the RTSA for various stimuli.....	53
Figure 3-27: Gamma-ray well testing with the GEN-2 and SPDR.....	55
Figure 3-28: Neutron well testing with the SRR#1 and LiTaO ₃	55

TABLE OF TABLES

Table I: Electromagnetic measurements on dielectric and ferroelectric materials	17
Table II: Electromagnetic measurements on magnetic materials	18
Table III. Summary of XRD structure data for CoCr_2S_4 sample. The ICSD# denotes the number assigned to the pattern from the International Crystal Structure Database. The Ref. denotes the reference from which the data was obtained for the structure fits. “a, b, c” denotes the unit-cell size. The size listed is the crystallite size (in nm) calculated by Rietveld refinement of the unit cells. “m%” denotes the mass% of the phase determined through analysis by Topas 4.2.	28
Table IV. Summary of XRD structure data for CdCr_2Se_4 sample. β is the beta-angle in the unit cell. See Table III for a description of the other column headings.	28
Table V: Resonant cavity characteristics	42
Table VI: Resonant cavity dimensions	43
Table VII: Material measurements using resonant cavities	43
Table VIII: Materials and resonator parameters for GEN-1 feedback amplifier sealed source testing	47
Table IX: Sealed sources used for GEN-1 feedback amplifier testing	48
Table X: GEN-1 feedback amplifier sealed source testing exposures	48
Table XI: GEN-2 feedback amplifier resonator parameters	50
Table XII: SRR feedback amplifier parameters	51
Table XIII: Button sealed sources used	52
Table XIV: Summary of stimulus tests for resonator; an X placed in the γ or n column indicated that they were tested with sealed sources	53
Table XV: Samples tested with well sources for high dose-rate testing	55

1 Executive Summary

The overarching objective of this project was to assess the effects of ionizing radiation on at least three classes of electromagnetic materials. The proposed approach for radiation detection was to utilize radiation-induced changes in dielectric permittivity, magnetic permeability, or electrical conductivity and their effects on resonant cavities. The resonant cavity circuit was envisioned as being remotely placed on a radio-frequency identification (RFID) tag, near a radioactive source that was desired to be monitored remotely. Microwave or low millimeter wave electromagnetic radiation would be used to interrogate the device through a simple power reflection change or other more sophisticated designs.

This project has resulted in eleven journal publications to date. The project explored radiation-sensitive arsenic sulfide glasses, ferroelectric oxides, and various magnetic materials including oxide permanent magnets, low coercivity oxide magnets, spin glass magnets, core-shell nanoparticles, and magnetic semiconductor chalcogenide materials. Working in parallel, the team performed radiation testing in the resonator on commercially available materials.

Year 1 of this project focused on modeling, measurement, and device design. Aspects of system design, material selection, and material testing were performed. Highlights on the system design included: refinement of system concepts; simulation and sensitivity study of cavity performance under changes in permittivity and permeability; testing of three resonant cavity designs; and design and fabrication of a feedback amplifier for transient measurements. Highlights on the material selection and testing included: measurement of electromagnetic properties of >30 materials; identification of ~10 materials for further study; synthesis of 4 materials of interest; irradiation testing using high dose ^{60}Co of 3 materials and ion irradiation of 1 material; and demonstration of permanent irradiation-induced changes in 1 dielectric ($\text{As}_x\text{S}_{1-x}$ glass) and 2 magnetic materials (Fe_3O_4 nano-granular film on Si, $\text{BaFe}_{12}\text{O}_{19}$ powders).

Year 2 of the project was directed towards discovery, fabrication, and testing of electromagnetic materials which respond selectively to different types of radiation. There was also an increased emphasis on design, fabrication, and testing of a device that can monitor near real-time changes in electromagnetic properties as may be expected due to radiation interaction. First, candidate materials were selected, characterized, and fabricated for loaded resonator testing. Commercial materials were obtained spanning obvious materials classes for consideration: semiconductors (high resistivity Si wafers), insulators (lepidolite mica, phlogopite mica), ferroelectrics (LiNbO_3 wafers), and magnetic insulators ($\text{BaFe}_{12}\text{O}_{19}$ hard magnets, $\text{Y}_3\text{Fe}_5\text{O}_{12}$ soft magnets). The geometry of other candidate materials available commercially was not conducive to testing their radiation sensitivity in the available devices.

In the middle of year 2 of the project, more focus was applied to device development and the material activities were centered on providing form-factored detectors to test in the resonators. The device component of the project proceeded on several levels as well. The original design (GEN-1) for this device was a feedback amplifier, consisting of commercially

purchased resonator cavities (split post dielectric resonator for dielectric permittivity or dielectric ring resonator for magnetic permeability), a feedback amplifier circuit, a mixer and frequency down-conversion circuit, and an output monitor using a standard swept spectrum analyzer or oscilloscope with a trigger point. This configuration was tested with ~ 5.7 mCi ^{137}Cs and ~ 60 μCi ^{252}Cf sealed sources with these two resonator types and four different materials. The primary lessons learned from this set of tests were centered around the fact that the exact signature of radiation interaction was unknown, so other environmental factors had to be highly controlled and data had to be monitored on a near real-time basis (faster than sweep rates >50 ms for standard spectrum analyzer).

These improvements were incorporated in the second generation (GEN-2) feedback amplifier system in year 3. In this system, the thermal stability was improved by separating the resonator plate from the amplifier plate and using a controlled thermo-electric cooler block with the resonator. For visualizing the output data, a real-time spectrum analyzer was leased, which provided 292,000 samples per second at frequencies high enough that the frequency down-conversion plate was no longer required and thus the feedback resonator test configuration was greatly simplified. This configuration was tested with ~ 100 μCi ^{137}Cs and ~ 30 μCi ^{252}Cf sealed sources with three different resonators (the two used previously plus a split ring resonator) and six different materials. Transient signatures were clearly identified for environmental phenomena (thermal drift, vibration, human proximity, room lighting) as well as deliberate stimuli (laser illumination, flash lamp, hand-held magnet).

The effect of gamma and neutron irradiation using the above sealed sources was difficult to ascertain since the exact phenomenology of the expected signature was still unknown. To attempt to conclude whether the lack of changes was due to dose rate, a further set of tests was conducted using PNNL's "well room" where a ~ 20 Ci ^{137}Cs source can be used to provide gamma dose rates up to ~ 0.1 Gy/hr and a ~ 7.5 mCi ^{252}Cf source can be used to provide neutron dose rates up to ~ 2 mGy/hr. The preliminary conclusions to this point are that Si showed the best sensitivity to gamma radiation and a frequency shift was measurable at the highest dose rates. Other samples showed profound sensitivity to uncontrollable well configuration parameters such as translation of the source from the 30 foot deep well via stepper motor and movement of a lead shield. This project explored a number of different candidate material systems and electromagnetic material change mechanisms. The key insight from this work is that, for small radioactivities and at room temperature, it is very difficult to perceive small changes in electromagnetic materials in the resonant cavities used here. Part of this involved the relatively small volumes of detector material used compared to many conventional radiation detectors.

Another way to conceive of the discovered sensitivity the resonator system to various environmental perturbations, as described above, is as an elegant platform for creating a variety of sensors. The sensor system is composed of a resonant circuit with a component which is sensitive to a desired perturbation. The circuit consists of a cavity resonator placed in the positive

feedback path of a microwave amplifier. An electromagnetic material placed inside the cavity resonator acts as the transducer and interacts with the desired environment. Depending upon the material type and resonator configuration, the detector output has demonstrated sensitivity to human proximity, acoustic vibrations, electromagnetic fields, light, or temperature. A primary benefit of this design is that it can provide very sensitive responses due to the high dynamic quality factor of the system. Proof-of-concept prototypes have exhibited dynamic Q-factor values as high as 15 million. Integral to the device operation is the ability to wirelessly transmit the time-dependent resonant signal. With appropriate development, this device could be used as a remotely placed wireless sensor to monitor and transmit data to another location. Based on this concept, a US Patent application has been filed.

2 Technical approach

Traditional solid state radiation detectors operate by counting charge carriers (semiconductors) or optical photons (scintillators) resulting from ionization events occurring in the materials. The requirement of co-located detector material and signal readout electronics in conventional detection architectures typically limits the range of these methods for standoff applications due to attenuation and down-scatter of characteristic gamma rays. In an alternative approach, the detector material and the readout mechanism are decoupled and the detector material is assumed to be co-located with the radiation source. This detection paradigm mitigates the inherent range limitation due to atmospheric transport of gamma rays. Feasible techniques for contactless standoff remote monitoring of the detector must be identified and implemented for this method of radiation detection to be successful. We propose an alternate strategy whereby the detector is proximal to the radiation source, and the readout apparatus remotely interrogates the detector material from a substantial standoff by electromagnetic waves at microwave or millimeter-wave frequencies. Initial models have been created assessing the gamma interaction in some potential alternative detector materials whose operation may not involve direct charge counting or scintillation. These materials may have utility for radiation detection, but have been overlooked as traditional detector materials due to excessively large bandgaps, poor charge transport properties, and magnetism.

2.1 Detection concept

Ionizing radiation creates a transient change in the population of free charge carriers in a material. This change in free carrier population induces three other subsequent electromagnetic (EM) property changes: 1) a change in electrical conductivity (a form of dielectric loss); 2) a change in dielectric permittivity as the free carriers couple with electric dipoles; and 3) changes in magnetic permeability as the free carriers couple with electron spins in magnetic dipoles. Ionizing radiation can produce both transient and permanent changes in these EM properties (see Figure 2-1), the former of which is expected to have greater magnitude. Studies in the literature have focused on two very different aspects of this problem: identifying permanent EM changes with radiation due to the greater ease of experiments, and finding materials that are insensitive to radiation (e.g. for space exploration applications, satellites.)

In one possible concept for a standoff radiation detector, a change in reflectivity as a function of radiation dose is observed (Figure 2-2). Similar constructs have been proposed for standoff chemical sensing platforms; the presence of the target compound induces a change in absorbance of the material, and hence a change in reflectance (Bray et al. 2008). Sensitivity can be improved by designing a resonant structure, in which a change in its frequency indicates the presence of the chemical (Bray et al. 2007). Similar designs have been suggested for radiation detectors where a resonant circuit is used which has at least one element that changes its properties (resistance, inductance, or capacitance) in response to irradiation (Burger et al. 2007).

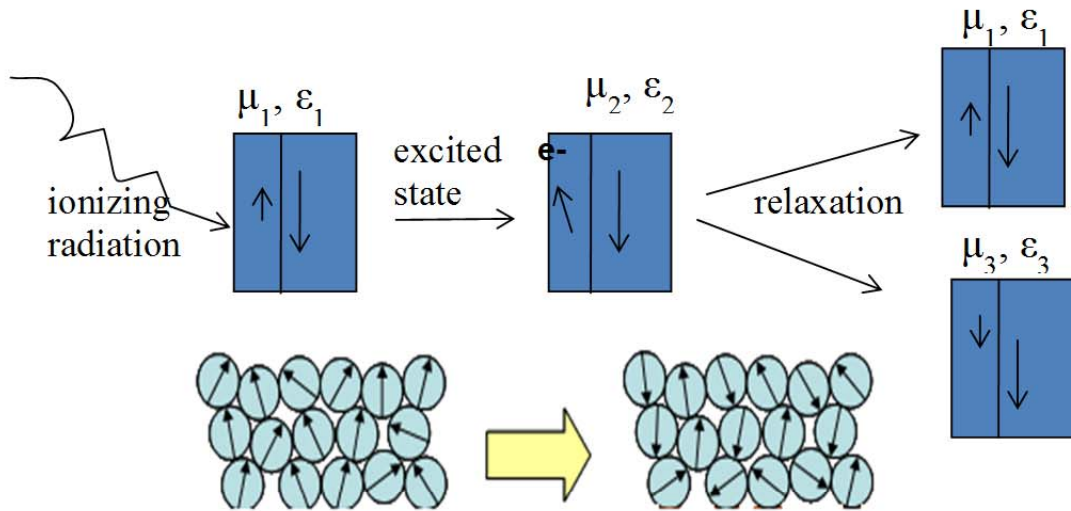


Figure 2-1: Concept for radiation-induced transient or permanent change in the magnetic permeability (μ) or dielectric permittivity (ϵ)

Two notable examples of recent work by other groups illustrate aspects of this concept. First, the UCSD/Spawar/VCU group has shown room temperature detection of gamma-radiation through power reflection change of a cavity containing Cd-Zn-Te (Cetinoneri et al. 2010). In essence this experiment showed a reduction in cavity quality factor (Q factor = resonant frequency/ full-width-half-maximum of absorption) due increased conductivity from the electrons created by the ionizing radiation. Using a $1 \mu\text{s}$ time constant preamplifier, the decay of the conductivity could be monitored as a transient. Second, the group at Pennsylvania State University (Mayer 2010) has been investigating using frequency shifts of resonant structures due to electron or neutron irradiation. In this case only a permanent change is monitored due to an increase of permittivity of a polymer creating an increase in capacitance in the resonant structure.

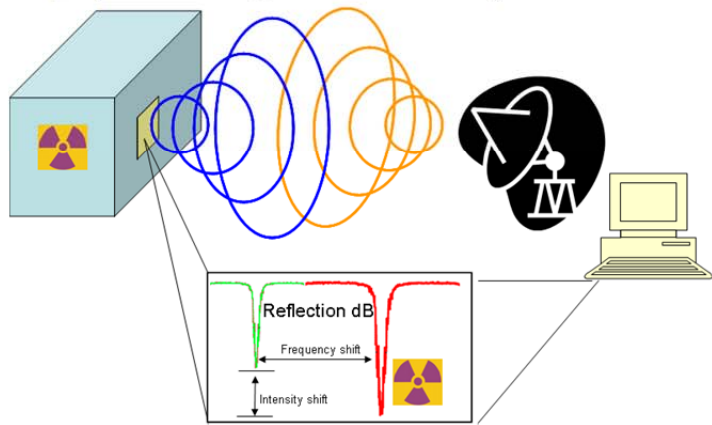


Figure 2-2: One possible concept of operations for the radiation detector

It is generally accepted that power reflectivity changes of 0.05 decibels are readily detectable by current commercially available microwave/millimeter-wave transceivers. This amount of power change corresponds to a 1% change in reflectivity. Power reflectivity (R) of a

surface in contact with air is a function of wave impedance of the medium ($\hat{\eta}$) and of free space (η_0) (Pozar 2005).

$$R = \left| \frac{\hat{\eta} - \eta_0}{\hat{\eta} + \eta_0} \right|^2 \quad \text{Equation (1)}$$

The impedance of free space is $\eta_0 = \sqrt{\mu_0/\epsilon_0} = 120\pi = 377\Omega$, while the impedance of the medium can be described as (Harrington 2001)

$$\hat{\eta} = \sqrt{\frac{j\omega\hat{\mu}}{\sigma + j\omega\hat{\epsilon}}}. \quad \text{Equation (2)}$$

Here j is $\sqrt{-1}$, ω is the angular frequency ($= 2\pi \times$ frequency in Hz), $\hat{\mu}$ is the complex magnetic permeability, $\hat{\epsilon}$ is the complex dielectric permittivity, and σ is the electrical conductivity. The complex permeability and permittivity are formally described as

$$\hat{\mu} = \mu' + j\mu'' = \mu_0 (\mu_r' + j\mu_r'') \text{ and } \hat{\epsilon} = \epsilon' + j\epsilon'' = \epsilon_0 (\epsilon_r' + j\epsilon_r''), \quad \text{Equation (3)}$$

where the quantities of subscript zero are the free space values ($\epsilon_0 = 1/36\pi \times 10^{-9} \text{ F/m}$; $\mu_0 = 4\pi \times 10^{-7} \text{ H/m}$) and those of subscript r are the relative values (unitless and usually quoted). It can be seen from Equation (2) that changes in the permittivity, permeability, and conductivity all affect the reflectivity, and it is expected that the free-carrier population may change either the real and/or imaginary components of the permittivity and/or permeability in addition to the normally assumed conductivity change.

2.2 *Radiation sensitive materials*

For the case of a material where ionizing radiation only causes a change in its electric permittivity (ϵ), the need to create a 1% change in reflectivity requires a 5% change in the dielectric constant (e.g., $\epsilon' = 9.5 \rightarrow 10$) which may be difficult to achieve in most materials without large doses. There are materials, however, that may display a higher sensitivity to ionizing radiation due to changes in their magnetic permeability. For example, the soft magnetic material $\text{Y}_3\text{Fe}_5\text{O}_{12}$ (YIG) undergoes a change in μ_r' at 7.85 GHz from 0.802 to 0.995 with the addition of a small magnetic bias that can be supplied by a hand magnet. This small perturbation results in a 24% change ($\Delta\mu_r'/\mu_r'$) in real permeability and consequent 4% reduction in reflectivity. For this calculation $\epsilon_r' = 14.4$ and ϵ_r'' , μ_r'' , and σ are small enough that they can be ignored. It seems, then, that realizable changes in magnetic permeability, which may be achievable with ionizing radiation, have a great enough magnitude to be seen using a simple reflection measurement.

Various other materials have been shown to have permanent changes in electromagnetic properties when exposed to radiation. Permanent conductivity changes in spinel oxide ferrites after exposure to gamma rays have been used to explore conduction mechanisms (electronic versus vacancy), charge transfer, and trapping dynamics (Mousa et al. 1989). Small permanent permittivity changes have been observed in large bandgap crystalline dielectrics such as alumina

and beryllia and larger changes in thin film and ceramic ferroelectric PZT (lead zirconium titanate) after irradiation with gamma rays or neutrons (Edelson et al. 1969; Sternberg et al. 2003; Sternberg et al. 1997). Non-intuitive decreases in loss tangent along with decreases in dielectric constant and some amorphisation were shown with Li⁺ ion-irradiated PZT thin films (Angadi et al. 2003b). Capacitance of phlogopite mica has been shown to be highly sensitive to neutrons (cGy doses) yet insensitive to gamma rays (kGy doses) (Roy and Pandya 2005). Magnetic permeability decreases have been observed in oxide spinels and garnets after irradiation with x-rays, gamma-rays, and neutrons (Hisatake et al. 1974; Hisatake et al. 1992; Parkhomenko et al. 1976). Also, various experiments involving ion irradiation in magnetic oxide garnets, hexaferrites, and spinels have shown substantial changes in magnetization and Mossbauer spectra due to creation of paramagnetic channels, which could usually be removed with annealing (Heitmann and Hansen 1984; Jin et al. 1996; Toulemonde et al. 1987; Costantini et al. 1995; Studer et al. 1993; Meillon et al. 1996).

Some transient EM property changes due to irradiation have been described in the literature. Photoconductivity has been reported for Ge and CZT (cadmium zinc telluride) in resonant cavities excited with 4 MeV x-rays and measured using reflected microwave power (4 – 10 GHz) (Tepper and Losee 2001). Single photon event, pulse, and energy scaling measurements were performed to evaluate detector linearity for spectroscopic applications (Tepper and Losee 1997). Edelson et al. (Edelson et al. 1969) have observed a distinct transient response in the dielectric loss tangent (1-12 GHz) of MgO after irradiation by neutrons or gamma rays.

The change in magnetic permeability and frequency of the spin resonance in some material is sensitive to radiation exposure. A photomagnetic response of oxide spinel ferrites and garnets has been investigated with excitation from visible, infrared, x-rays, and gamma rays (Metselaar and Huyberts 1974; Hisatake 1977; Chizhik et al. 1998; Hisatake et al. 1992; Hisatake et al. 1974). In the photomagnetic effect, the magnetocrystalline anisotropy field due to electron redistribution among multiple nonequivalent lattice sites changes as a result of inter-valence charge transfer (IVCT), usually of $\text{Fe}^{3+} \rightarrow \text{Fe}^{2+}$ on octahedral sites (Teale and Temple 1967b; Teale et al. 1970) or between $\text{Fe}^{3+} \rightarrow \text{Fe}^{2+}$ and other multivalent ions ($\text{V}^{3+} \rightarrow \text{V}^{4+}$, $\text{Mn}^{2+} \rightarrow \text{Mn}^{3+}$) (Metselaar and Huyberts 1974). Relaxation times for the photomagnetic effect in YIG:Co (Stupakiewicz et al. 2001) and YIG:Si (Wurlitzer 1981) involve multiple recombination centers and depends strongly on the electronic structure. Some dynamic magnetization studies have been carried out using femto-second lasers showing the time scales of spin-electron and spin-lattice relaxation (Ogasawara et al. 2005). The photomagnetic effect has also been shown to result in a decrease in permeability due to domain wall pinning and prevention of the magnetic field from storing energy by moving the domains. Similar mechanisms of domain wall pinning have been observed for magnetic changes due to neutron degradation in structural metals, and these changes have been used as a nondestructive evaluation techniques for monitoring nuclear power plant materials (Dobmann 2006).

2.3 Preliminary material selection

Selection of materials for study was influenced by the reports of unusual effects on electromagnetic properties when excited by radiation, usually optical or infrared frequencies. It is postulated that some aspects of these effects will be seen with higher energy excitation by x-rays and gamma rays. Materials chosen were those which showed either ferroelectric or magnetic properties.

PMN-PT ($0.7\text{Pb}(\text{Mg}_{1/3}\text{Nb}_{2/3})\text{O}_3\text{-}0.3\text{PbTiO}_3$) is a very dense high dielectric constant relaxor ferroelectric with complicated nanophase structure (Carter and Norton 2007). PMN-PT is of interest to this study because Li^+ ion irradiation of 80PMN-20PT (similar composition) has been shown to increase the dielectric constant and loss tangent, presumably by permanent disturbance of the nanophase clusters and chemical inhomogeneities that characterize a relaxor ferroelectric (Angadi et al. 2003a). Ferroelectrics LiTaO_3 (LT) (Chao and Hung 1996) and LiNbO_3 (LN) (de Almeida et al. 2006) have both shown changes in electrical domains with optical irradiation.

Similarly, some soft ferrimagnets with low coercive fields have shown the presence of the photomagnetic effect, where magnetocrystalline anisotropy field and bulk permeability changes upon irradiation. YIG has been studied extensively in this regard (Teale and Temple 1967b; Metselaar and Huyberts 1973; Metselaar et al. 1975; Hisatake et al. 1992; Chizhik et al. 1998), but $\text{Gd}_3\text{Fe}_5\text{O}_{12}$ (GIG) has also showed promise in this arena (Hisatake and Matsuyama 1974), and has higher density than YIG with the added bonus of Gd atoms which have high Z and high neutron cross-section. Both Ba-M and Co₂z hexaferrites, being permanent magnets, exhibit relatively low magnetic losses in the microwave region due to their high frequency spin resonance in the millimeter-wave (MMW) region (Smit and Wijn 1959). Nickel ferrite (NiFe_2O_4 or NF) has a resonance in MMW but has more loss at lower frequencies than the permanent magnets (Chen et al. 2009). CdCr_2Se_4 (CCS) is a magnetic semiconductor with a spinel structure that also has shown interesting photomagnetic properties (Lems et al. 1968; Mosiniewicz-Szablewska and Szymczak 1993). Finally, $\text{Cd}_x\text{Mn}_{1-x}\text{Te}$ (CMT) is a large bandgap semiconductor similar to CZT, which also is being considered for traditional radiation detectors (Burger et al. 1999; Parkin et al. 2007); in addition, CMT is a dilute magnetic semiconductor that has shown some photo-induced magnetic effects (Furdyna 1988; Smith et al. 1994).

It is conceivable that a combination of these materials could be exploited to form a type of spectroscopic radiation detector in which spatially dispersed regions of the detector surface and/or interior volume are tuned for maximum sensitivity to specific portions of the ionizing radiation spectrum (i.e. a “radiation nose” system (Arshak and Korostynska 2006)). Other inhomogeneous material configurations can be imagined which take advantage of the radiation-induced changes in carrier concentration that may affect electromagnetic properties such as dielectric permittivity and magnetic permeability.

2.4 Potential applications

Depending on the lifetime of the carriers in the material and the carrier generation rate due to the radiation source (and other sources such as thermal), the material could end up in one of three operational limits analogous to other radiation detectors.

A. Low Rate Limit: “Pulse counting mode”

The radiation source is weak and/or the carrier lifetime in the material is very short. In this case, the signal in the material has completely or at least substantially diminished by the time the next event reaches the active material. In this way, a set of statistics are generated describing the number of electrons created versus integration time bin.

B. High Rate Limit: “Current mode”

Here the radiation source is strong and has perhaps “saturated” the active material. In this case, it might be more useful to have a material which does not totally saturate but continues changing its accessible properties with increasing dose. Here the electrons do not relax fast enough before more are created, and the signal is more or less a cumulative average of the ionization events. The signal is thus proportional to the power deposited in the material, requiring *a priori* knowledge of either activity or isotope for proper identification. This limitation may not be critical for some applications, since remote monitoring of spent fuel, for instance, would presumably provide some knowledge of what material is in the canister.

C. Permanent changes: “Integrated dose mode”

It may be that some electromagnetic changes are a) permanent and b) very dose dependent. These types of changes could be used as monitors for exposure. For example, $\text{Bi}_4\text{Ge}_3\text{O}_{12}$ (BGO) films have shown a linear increase in capacitance after the threshold of ~ 1.8 mGy was reached (Arshak et al. 2008). Likewise, there are many other examples in both ferromagnetic (Parkhomenko et al. 1976) and ferroelectric (Sternberg et al. 2003) materials in which radiation-induced changes were quasi-permanent until annealed at high temperature.

2.5 Specific approach to this project

In this project, the goal is to explore multiple classes of materials for magnetic and/or dielectric changes and transient and/or permanent effects. Some basic electromagnetic properties were measured as a screening for potential radiation-sensitive materials. Resonant cavity testing was performed on selected materials. Later testing was performed after or during irradiation by γ -rays, ions, and neutrons. Radiation induced permanent and/or transient changes were measured during/ after irradiation. Ultimately it was hoped that some non-contact method of interrogation could be demonstrated on a lab scale.

3 Technical highlights

3.1 Detector materials

Below is a summary of some of the material evaluation and development conducted under this project. Where journal publications resulting from this project were not submitted, a more detailed description is provided. Where publications were made, only a summary and reference are provided. Some of the materials below were investigated as a function of irradiation. Others are included to acknowledge the rationale that went into pursuing them as radiation detector materials. Publications were not prepared in all cases.

Since in this project we wanted to put some additional focus on magnetic changes with irradiation, as part of the project we purchased an AC magnetic susceptibility (ACMS) option for our existing Physical Property Measurement System (PPMS, Quantum Design). The ACMS in conjunction with the PPMS allow measurement of frequency dependent magnetic susceptibility (permeability) from 10 Hz to 10 kHz in addition to providing standard DC magnetic measurements, all as a function of temperature 2K – 350 K and at magnetic fields up to 9 T. A large number of samples were screened with this instrument to look for candidate frequency dependent behaviors that could possibly be exploited as sensitive indicators of environmental perturbation (i.e. radiation). A few samples were tested using Far-infrared reflection from 20 – 700 cm⁻¹. A comprehensive list of the materials and measurements is provided in Table I for dielectrics/ ferroelectrics and Table II for magnetic materials. Additionally, a number of materials were tested with room temperature millimeter wave transmission (and in some cases reflection) measurements, as a function of frequency from 30-120 GHz (Tufts) and 180-260 GHz (PNNL) (McCloy et al. 2011b).

Table I: Electromagnetic measurements on dielectric and ferroelectric materials

Materials tested	Microwave cavity 8 GHz	MMW 30-120, 180-260 GHz	Far-IR	Project Publications
Si (high resistivity)	10 wafers	Too thin for fringes		
PZT on Si	X			
BaTiO ₃ on Si	X	Too thin for fringes		
LiNbO ₃	3 orientations	3 orientations	1 orientation	(McCloy et al. 2011b)
LiTaO ₃		3 orientations	1 orientation	(McCloy et al. 2011b)
Mica, phlogopite	X	Too thin for fringes		
Mica, lepidolite	X			
BaTiO ₃		3 compositions	X	(McCloy et al. 2011b)
SrTiO ₃		X	X	(McCloy et al. 2011b)
PMN-27/32-PT		X	X	(McCloy et al. 2011b)
LaAlO ₃		X		(McCloy et al. 2011b)
Bi ₃ Ge ₄ O ₁₂		X		(McCloy et al. 2011b)
As S _x S _{1-x}		5 compositions	1 composition	(McCloy et al. 2010)
Ag ₃ AsS ₃				

Table II: Electromagnetic measurements on magnetic materials

Materials tested	DC susceptibility	AC susceptibility (10 Hz – 10 kHz)	Microwave	Other	Project publications
$\text{Y}_3\text{Fe}_5\text{O}_{12}$	Ceramic	Ceramic	6, 7, 8 GHz, demag & sat	γ -irradiated; far-IR	
CVG YIG			8 GHz, demag & sat		
$\text{Gd}_3\text{Fe}_5\text{O}_{12}$	Powder	Powder			
$\text{BaFe}_{12}\text{O}_{19}$	5 powders	2 powders	Ceramic – 2 GHz	γ -irradiated; far-IR	
Fe_3O_4	~10 powders	~3 powders			
Fe_3O_4 granular on Si	X			Ion irradiated	(Jiang et al. 2011)
FeO/ Fe_3N granular on Si	X	X		Ion irradiated	(Sundararajan et al. 2011)
Fe core/ Fe_3O_4 shell granular on Si	X			Ion irradiated	
$\text{Cd}_{1-x}\text{Mn}_x\text{Te}$	4 compositions	4 compositions		EPR 9.4 GHz; Far-IR on 5cat%	
CoCr_2S_4	Powder	Powder			
CdCr_2Se_4	Powder	Powder			
FeTiO_3	Powder	Powder			
Fe_2O_3	Powder	Powder			
$\text{La}_{0.8}\text{Sr}_{0.2}\text{MnO}_3$	Powder	Powder			
La_2CuO_4	Powder	Powder			
$\text{Ni:Co:CuMn}_2\text{O}_4$	4 compositions	4 compositions			(McClay et al. 2012)
NiCo_2O_4	Powder	Powder			
Metals	3 (Fe, Pd, Permalloy)	2 (Fe, Pd)			

Following is a more detailed description of a few of the most important materials or material systems evaluated in this project for their use as new radiation detectors based on electromagnetic material property changes.

3.1.1 $\text{As}_x\text{S}_{1-x}$ semiconducting glasses

$\text{As}_x\text{S}_{1-x}$ glass was chosen for irradiation testing because of its known refractive index (i.e. dielectric permittivity) change to visible and infrared light. Additionally, PNNL has experience with this system and can produce it in our Nonoxide Materials Synthesis Laboratory (McClay et al. 2010). Our hypothesis was that the As-S glass would be similarly susceptible to gamma radiation as it is to visible light.

The As-S samples were irradiated to 1, 2, 3, and 4 MGy at 2.8 Gy/sec. After each radiation step, the refractive index was measured at 633 nm using a prism coupler (Meticon), with a precision of 0.0001 on the refractive index. Additionally, the energy gap (via UV-VIS transmission spectroscopy), Raman spectrum, and 180-260 GHz refractive index were obtained after each dosing. X-ray diffraction was performed on samples after 3 and 4 MGy. These data

were compared to previous data taken on these samples from 1 year ago, as well as “aged” samples (same batch but relaxed in the dark for 1 year). The results suggest that the irradiation produced structural rearrangement and bond breaking, leading to an increase in refractive index which is almost linear for most compositions.

We published these irradiation results on refractive index recently (Sundaram et al. 2012). Leading up to the aforementioned work and as a part of this DTRA program, we have collaborated on two papers on irradiation effects on thermal properties (Golovchak et al. 2011; Lucas et al. 2011) and one on the structure of these materials (Golovchak et al. 2010).

3.1.2 $\text{BaFe}_{12}\text{O}_{19}$ magnets

Little is currently known about the effects of gamma-ray irradiation on oxide magnet materials. In particular, the effect of particle size on radiation susceptibility was investigated. Two commercial powders of $\text{BaFe}_{12}\text{O}_{19}$ (micrometer size and nanometer size) were thoroughly characterized, then exposed to 1 MGy of gamma radiation from a ^{60}Co source. AC susceptibility and DC magnetometry and Mossbauer spectroscopy were performed after irradiation and compared to pre-irradiated measurements. DC magnetization and AC susceptibility decreased for both samples with the relative change of DC magnetization being larger for the micrometer-sized particles and the relative change of the AC susceptibility being larger for the nanometer-sized particles. Mossbauer spectroscopy indicated a decrease in both the hyperfine fields and in their distribution for each Fe site, particularly in the larger particle sample. Decreases in susceptibility are believed to be due to radiation-induced amorphization at the particle surfaces as well as amorphization and nucleation of new crystallites at internal crystallite boundaries, resulting in overall reduction in the particle magnetic moment. This radiation damage mechanism is different than that seen in previous studies of neutron and heavy ion irradiation of $\text{BaFe}_{12}\text{O}_{19}$. These results were recently published (McCloy et al. 2011a).

Millimeter-wave absorption (30-120 GHz) was measured using a backwards wave oscillator (BWO) for micro- and nano- hexaferrites, and the latter shows a much lower absorption frequency (Korolev et al. 2012). It is found that the absorption frequency likely depends on not only the volume fraction, but also the shape anisotropy and coercive field of the particles (paper submitted).

Reflection measurements were taken on bulk $\text{BaFe}_{12}\text{O}_{19}$ magnets to assess feasibility of performing a reflectance measurement at stand-off. The results were disappointing in that the reflectance spectrum in the ferromagnetic resonance (FMR) band (45 – 65 GHz) appeared to be just a reflectance from the front side with the rest being absorbed, and similar to what the detector records from the bare BWO. At higher frequencies there is little change in transmittance or reflectance as expected. In summary, the reflectance spectrum was not as informative as the transmittance spectrum, though possibly could still be used, but quantifying small changes in the reflectance spectrum of a system with this broad of a FMR would be challenging. Nanopowders, however, have a much narrower resonance (Korolev et al. 2012) and

hence may be more suited to assessing radiation-induced changes. Unfortunately, we were not able to irradiate sufficient powder to take BWO measurements on irradiated samples.

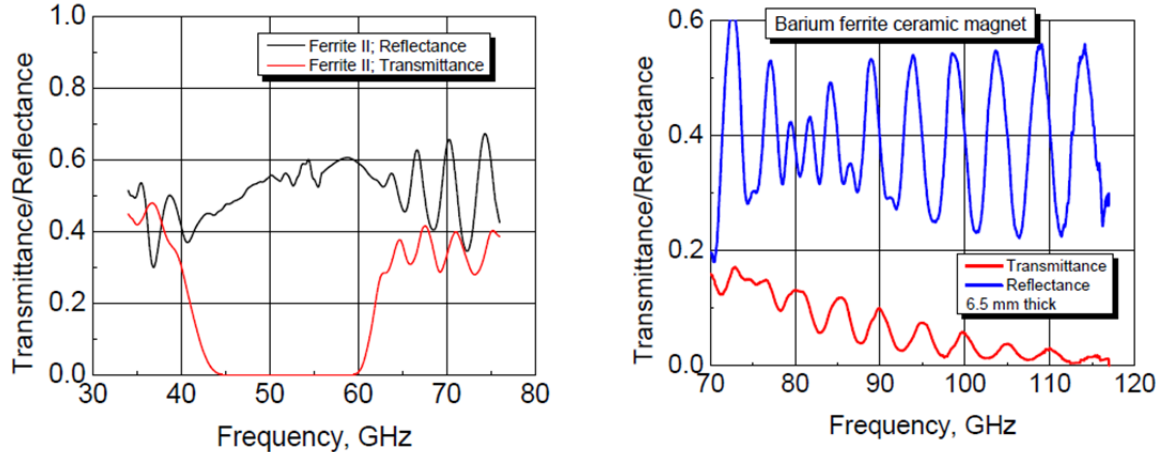


Figure 3-1: Bulk $\text{BaFe}_{12}\text{O}_{19}$ commercial ceramic magnets (McMaster Carr) backwards wave oscillator transmittance and reflectance measurements in the (a, left) Q band (33-50 GHz) and V band (50-70 GHz) and the (b, right) W band (75-110 GHz).

3.1.3 Granular Iron oxide films

We have explored some very interesting magnetic nanostructures made by the University of Idaho which, depending on their composition, either exhibit no change (Sundararajan et al. 2011) or dramatic change (Jiang et al. 2011) in their magnetic properties with ion irradiation. Some of the University of Idaho graduate students continue to work with these materials and we have new collaborators at the University of California Davis who are using a technique known as First Order Reversal Curve (FORC) (Roberts et al. 2000) to further analyze the radiation-induced changes in these materials. We anticipate further publications in this area, and it should be noted that DTRA funding was key in putting the right collaboration together on this initially. These materials were found to exhibit dramatic irreversible changes, which could be useful for anti-tamper or other applications. We reproduce the abstract of our first paper in this area below (Jiang et al. 2011).

Porous granular films of magnetite (Fe_3O_4) with grains of ~ 3 nm in size were prepared using a state-of-the-art nanocluster deposition system. The films are initially superparamagnetic but become magnetized following Si^{2+} ion irradiation. A significant increase in the grain size and a dramatic change in the microstructure are observed. There are dipolar interactions between the nanoparticles in both the unirradiated and irradiated films. The in-phase alternating current magnetic susceptibility of the unirradiated film shows a blocking temperature of ~ 150 K, depending on frequency. A broadened Verwey transition for the irradiated film occurs at ~ 75 K, above which the susceptibility exhibits unusual behavior: a nearly linear decrease with decreasing temperature. There are irreversible domain rotations in the irradiated film during zero-field cooling and warming cycles between 10 and 300 K. The observed behavior of the

irradiated granular films is quite distinct from that of metallic nanostructures after irradiation, and is due to the dramatic change in microstructures.

3.1.4 $\mathbf{Cd_{1-x}Mn_xTe}$

Cadmium zinc telluride (CZT) has been shown to possess measureable σ changes induced by radiation when probed by microwaves (Tepper and Losee 2001), and is a known room temperature γ ray semiconductor detector. Cadmium manganese telluride (CMT) is a magnetic analogue to CZT which has also been explored as a radiation detector material and will allow evaluation of *coupling* between σ and μ changes induced by free carriers (Parkin et al. 2007).

Some CMT was obtained commercially (International Crystal) and radiation detector grade material (Mn = 5 cation %) was obtained from Brookhaven National Laboratory (Aleksey Bolotnikov, Yinneltech material). Optical and magnetic properties of single crystals of $\mathbf{Cd_{1-x}Mn_xTe}$ ($x=0.05, 0.25, 0.33, 0.50$) were investigated for their potential as non-traditional radiation detectors. Transmission measurements in the visible confirmed the band-gap expected by the composition. Far-infrared reflectance and backwards-wave oscillator transmission measurements investigated the zero-field optical properties near the phonon resonances. Electron spin resonance, magnetic susceptibility (field-cooled/ zero-field cooled), vibrating sample magnetometry, and magnetoresistance measurements show the different behavior from this material at different magnetic dopant levels.

We have presented this work at an American Ceramic Society conference in 2010 but have not yet published the results in a journal.

3.1.5 The photomagnetic effect (PME)

The general explanation for the photomagnetic effect (PME) is that charge transfer or valence exchange, usually of $\mathbf{Fe^{3+} \rightarrow Fe^{2+}}$ on octahedral sites (Teale and Temple 1967b; Teale et al. 1970) or between $\mathbf{Fe^{3+} \rightarrow Fe^{2+}}$ and other multivalent ions ($\mathbf{V^{3+} \rightarrow V^{4+}}$, $\mathbf{Mn^{2+} \rightarrow Mn^{3+}}$) (Metselaar and Huyberts 1974), is responsible for the light-induced changes in magnetic properties. The PME is generally thought to manifest in two ways, both of which could be useful for exploitation in radiation detectors.

- 1) change in magnetocrystalline anisotropy field due to electron redistribution among multiple nonequivalent lattice sites which could have the more anisotropic $\mathbf{Fe^{2+}}$. There is some indication that the anisotropy field *increases* by about 1.2% within one minute due to the PME, at least in YIG:Si at 4.2 K (Teale et al. 1970). Various processes with different relaxation times contribute to the FMR linewidth in Mg spinel ferrite which contains both $\mathbf{Fe^{3+}}$ and $\mathbf{Fe^{2+}}$, but the mechanisms were not well understood (Goswami et al. 1968). At 77 K, YIG:Si was observed to have a response time for the PME of 100 μ sec or less (Enz and van der Heide 1968). The effect in YIG:Si was found to be sensitive to the polarization of the exciting infrared light, lending support to the idea that it was a redistribution of

anisotropic centers that were involved (Teale et al. 1969). It was later found that not all samples showed PME sensitive to polarized light, and those that did not tended to have low doping levels, had a PME that persisted to higher temperature and was “irreversible” except by heating, and was described as being more related to the domain walls and the absorption coefficient at the excitation wavelength while still being related to the valence exchange (Teale and Weatherley 1973).

- 2) decrease in permeability due to domain wall pinning and prevention of the magnetic field from storing energy by moving the domains. Since the permeability in question is low frequency (<150 kHz but likely has effects at longer frequencies), often the inverse of the magnetic susceptibility is talked about as the “domain wall stiffness” which increases with the PME, and the change of which is thought to be proportional to the number of class II defect centers (Enz et al. 1969) or the square root of the number (Lems et al. 1970). In some materials (Ca-V-garnets), the very high permeability is due to rotation contributions which are not affected by the PME, so even though the permeability is high, the change is small (Metselaar and Huyberts 1974).

The source of the hopping electron in YIG giving rise to the anisotropic Fe^{2+} can be compensation for doping with 4+ ions (Si, Ge, Zr, Ti)(Metselaar and Huyberts 1974) or some oxygen vacancies (Hisatake et al. 1992). The PME has been described in GIG as well (Metselaar and Huyberts 1974; Hisatake and Matsuyama 1974). The PME has been observed in some magnetic oxide spinel ferrites and attributed to charge transfer between Fe and either Ni, Cu, Mn, or Co (Marais and Merceron 1974), and even Ru (Jonker 1974), but is not universally observed (Metselaar and Huyberts 1974). The PME has also been observed in FeBO_3 (Lacklison et al. 1971) and recently in $\text{Pr}_{0.5}\text{Ca}_{0.5}\text{MnO}_3:\text{Cr}$ (Okimoto et al. 2002).

Nagaev (Nagaev 1988) explains the phenomena of PME differently, referring to a quasi-particle called a *ferron* which consists of an electron and a ferromagnetic (FM) micro-region. Rather than being simply a charge transfer of one electron between Fe^{2+} and Fe^{3+} , quantum mechanically the extra charge is spread out over multiple sites, thus facilitating the creation of micro-domains. He refers to evidence for photo-induced effects in the Eu chalcogenides EuO (FM), EuS (FM), EuSe (antiferromagnetic or AFM), EuTe (AFM), and some rare earth chromates, ErCrO_3 , and EuCrO_3 , in addition to the garnets (referred to above) and CdCr_2Se_4 (see below).

There can be multiple physical means for photomagnetism in semiconductors, depending on the type of semiconductor (degenerate, nondegenerate) and state of the light (circular polarized, plane polarized, unpolarized). Circularly polarized light affects the *exchange* while plane polarized light effects the *anisotropy*. Photomagnetism can come from *free photoelectrons* (small effect on the order of 0.2 K shift of T_{Curie} and requires about $10^{18} \text{ e}^-/\text{cm}^3$), *trapped electrons* at local centers where traps are filled then free photoelectrons are generated (larger effect), or precipitation of insulator-to-metal *phase transitions*. In some materials, the metal-insulator transition is related to photomagnetism, where the insulating ferron state (FM

sphere in an AFM matrix) converts to a conductor (AFM sphere in FM matrix) by increasing the temperature or the field. Trapped electrons can cause lattice constant changes which affect the f-f electron exchange energy and increase the local ferromagnetism, and magnetization increases with illumination. If the binding energy is small for electrons at traps, they are not really localized but “smeared out” over many sites promoting indirect exchange. This model is in contrast to the fixed position and valency exchange model proposed originally to explain the garnet PME.

A ferromagnetic chalcogenide spinel n-type semiconductor $\text{CdCr}_2\text{Se}_4:\text{Ga}$ having a Curie temperature (T_C) of 130 K was found to be more photosensitive than YIG by several orders of magnitude (Lems et al. 1968). Other related semiconducting Cr spinels besides CdCr_2Se_4 (RT $E_{\text{opt}} = 1.32$ eV), include CdCr_2S_4 (RT $E_{\text{opt}} = 1.57$ eV), HgCr_2S_4 (RT $E_{\text{opt}} = 1.42$ eV), HgCr_2Se_4 (RT $E_{\text{opt}} = 0.83$ eV), CoCr_2S_4 , FeCr_2S_4 , MnCr_2S_4 , ZnCr_2Se_4 (RT $E_{\text{opt}} = 1.28$ eV, AFM) (Wojtowicz 1969). Cu spinel structure magnetic chalcogenides of the formula CuCr_2X_4 and chalcohalides of the formula $\text{CuCr}_2\text{X}_3\text{Y}$ (where $\text{X} = \text{Se}^{2-}$, Te^{2-} and $\text{Y} = \text{Cl}^-$, Br^- , I^-) have been reported with Cu in tetrahedral and Cr in octahedral sites, though their valences have been debated (Robbins et al. 1968). All are room temperature ferromagnets with relatively high Curie temperatures, while the chalcogenides have metallic conductivity (CuCr_2S , $T_C=420$ K; CuCr_2Se , $T_C=431$ K; CuCr_2Te , $T_C=365$ K), but some of the chalcohalides appear to be semiconductors ($\text{CuCr}_2\text{Se}_3\text{Br}$, $T_C=274$ K, semiconductor; $\text{CuCr}_2\text{Te}_3\text{I}$, $T_C=294$ K; $\text{CuCr}_2\text{Se}_3\text{Cl}$, RT ferromagnet but hydroscopic). Also, $\text{CuCr}_2\text{S}_{4-x}\text{Cl}_x$ has been made which is a semiconductor with RT resistivity $8 \times 10^{-2} \Omega\text{cm}$ for $x \sim 1$ but here has $T_C \sim 200$ K whereas $T_C \sim 380$ K for $x \sim 0.1$ (Sleight and Jarrett 1968). Other chromium chalcogenide spinels (without copper, such as the cadmium chalcogenide spinels) are semiconductors with T_C well below room temperature (Robbins et al. 1968). Recently, a half-metallic magnetic copper chalcogenide CuV_2S_4 has been reported (Kumara et al. 2008).

Below a given characteristic temperature (150 K for YIG:Si, 30 K for $\text{CdCr}_2\text{Se}_4:\text{Ga}$ (Enz et al. 1970)), the effect lasts even after turning off the excited light. Above that temperature the “frozen in” state relaxes away (the permeability increases again) with some characteristic time that is not well known as a function of temperature. FMR experiments at 10 GHz on YIG:Si at 4.2 K indicate that this thermal relaxation time for the valence exchange is >100 fs at this temperature but less than ~5 minutes for most centers (Teale et al. 1970). For $\text{CdCr}_2\text{Se}_4:\text{Ga}$ at 77 K, the permeability has relaxed (increased) to its pre-illumination value within ~1 minute after turning off the excitation (Enz et al. 1970). These results suggest that the PME could be used for detection of multiple events if the temperature were high enough to thermally relax the effect prior to receiving another radiation event. There are two broad classes of the P. M. E. which are best described in (Metselaar and Huyberts 1974):

- Class I – “after effect type” involving some aspects of disaccommodation; considered “reversible” in that a demagnetizing field removes the decrease in permeability achieved in the PME; considered by most to involve defect centers close to Fe^{2+} ions. This type of

PME has been observed with excitation from x-rays and γ -rays in YIG with charged oxygen vacancies (Hisatake et al. 1992).

- Class II – “pure PME”; considered “irreversible” in that a demagnetizing field does not remove the decrease in permeability achieved in the PME; considered by most to involve defect centers far from the Fe^{2+} ions.

Disaccommodation is defined as the relaxation produced thermal or photo-energy, since after demagnetization, domain walls are not in minimum energy configuration (Metselaar and Huyberts 1974). In the case of thermal disaccommodation, the permeability *decreases* from a higher value achieved just after demagnetization.

In the case of photo disaccommodation, the permeability *increases* from a lower value produced by the photomagnetic effect. This is most easily seen in the following figure, taken from Ref (Metselaar and Huyberts 1974).

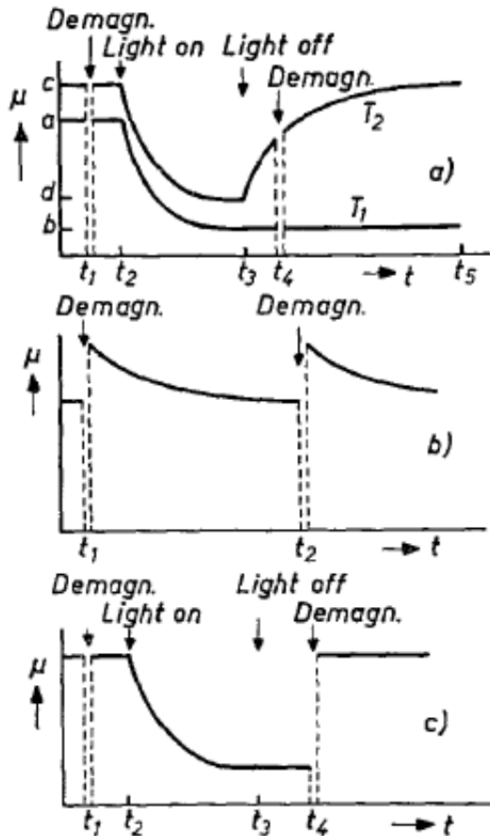


Figure 3-2: Permeability as a function of time showing disaccommodation processes (from Ref (Metselaar and Huyberts 1974)). (a) photo-induced effect of class II at two different temperatures; (b) thermally induced disaccommodation; (c) photo-induced disaccommodation

3.1.6 $\text{Ni,Co:CuMn}_2\text{O}_4$ spin cluster glasses

It was thought that spin glasses would show some magnetic changes with irradiation similar to that observed in the photomagnetic effect. In other words, irradiation with high energy

particles would create a shift in the spin freezing temperature similar to that seen with spin glasses like spinel cluster glasses (Seki et al. 2005a; Seki et al. 2005b) and Cd-Mn-Te (Kawai and Sato 1999). To that end, two spin glass classes were evaluated, but similar phenomena have been shown in the literature for many other systems.

First, we obtained some mixed cation magnetic spinels from a collaborator at University of Washington (Clifford Leslie). We characterized these samples and published one paper (see below) but were not able yet to perform photomagnetic (or radio-magnetic) effect measurements to look for changes in spin freezing behavior due to irradiation.

$\text{Mn}_{1.68}\text{Co}_{0.24}\text{Ni}_{0.48}\text{Cu}_{0.6}\text{O}_4$ was produced via slip casting and sintering of spray-pyrolysis produced powders. The magnetic properties of this composition were measured for the first time, as a function of the processing temperature (900 °C or 1000 °C sintering), in order to study the effects of Cu and Mn valence and site preference. Quantitative x-ray photoelectron spectroscopy showed that Cu^+ site occupancy changed from tetrahedral to a mix of tetrahedral and octahedral with increasing sintering temperature. X-ray diffraction demonstrated that the materials had a cubic spinel structure devoid of tetragonal Jahn-Teller distortion. ac magnetic susceptibility indicated ferrimagnetic behavior below ~109K and spin glass behavior below ~66 to 74 K, depending on the measurement frequency. ac susceptibility freezing temperatures were modeled with the Vogel-Fulcher law and showed intermediate characteristics, between those of canonical spin glasses and cluster glasses. This work was recently published (McCloy et al. 2012).

We have measured magnetic properties of several other compositions in this Ni-Co-Cu-Mn-O series and hope to publish these in the future.

3.1.7 $\text{Y}_3\text{Fe}_5\text{O}_{12}$ and rare earth garnets

The magnetic properties of rare earth iron garnets have made them attractive materials for uses ranging from optical communications to magnetic cooling (Srikanth et al. 2009). These materials are currents of interest for radiation detection due to the discovery of the photomagnetic effect in yttrium iron garnet (YIG) (Teale and Temple 1967a) and the potential addition of elements with high neutron cross-section (e.g. Gd) in the garnet structures. Additionally, rare earth garnets have three magnetic sublattices (two of Fe and one of the rare earth) resulting in a complex magnetization behavior with temperature resulting in a “compensation point” where magnetization is zero at a particular temperature (Valenzeula 1994). For $\text{Gd}_3\text{Fe}_5\text{O}_{12}$ this temperature is near room temperature (Heitmann and Hansen 1984), giving another possible mechanism for seeing small changes in compensation temperature due to perturbations such as irradiation.

Ceramic cylinders of commercial $\text{Y}_3\text{Fe}_5\text{O}_{12}$ (YIG) were exposed to 4 MGy of ${}^{60}\text{Co}$ γ irradiation and tested in the dielectric ring resonator (DRR) resonant cavity at 1 MGy increments. No changes in the 8 GHz complex magnetic permeability were noted. It is therefore

concluded that this polycrystalline ceramic YIG (obtained from Pacific Ceramics, YIG 39-1780CX) is very “rad hard” at least for permanent changes in high frequency permeability.

The only comparable literature we could find on this subject was one paper which showed the frequency dependent changes in YIG permeability with neutron irradiation (Podsekin et al. 1982), which showed that neutrons effected the high frequency permeability up to 10 GHz, but that changes were smaller as the frequency increased. Several other papers were located where YIG was tested with high doses of fast neutrons and the resulting structure and properties were measured (Chukalkin et al. 1983; Podsekin and Zaitsev 1982; Ubizskii et al. 1993; Ubizskii et al. 1996).

A summer student funded on the DTRA project synthesized and characterized five different garnet materials, yttrium iron garnet ($Y_3Fe_5O_{12}$, YIG), ($Gd_3Fe_5O_{12}$, GIG) and terbium iron garnet ($Tb_3Fe_5O_{12}$, TIG). To determine the effect of iron on the magnetic properties of these materials, gadolinium gallium garnet ($Gd_3Ga_5O_{12}$, GGG) and terbium gallium garnet ($Tb_3Ga_5O_{12}$, TGG) were also synthesized. Ac magnetic susceptibility of these materials was measured in both the demagnetized and remnant state. For TIG, GIG, and YIG, the real (χ') and imaginary (χ'') part of the ac susceptibility show variation with temperature and with frequency. For χ'' higher frequencies peak at higher temperatures, and the magnitude itself increases. These phenomena have not, to our knowledge, been reported before but are likely due to some glassy magnetic transitions involving interactions between the sublattices (Srikanth et al. 2009). Since the frequency dependence is in the YIG as well, at least some of the interaction is due to the interaction of the two Fe sublattices, though the magnetic (Gd, Tb) or nonmagnetic (Y) rare earth clearly has an effect on the spectra. We hope to publish these results in the near future.

3.1.8 Magnetic chalcogenide spinels

Chalcogen-based spinels (or chalcogenide spinels) are often reported in the literature for their unique and tunable magnetic, magnetooptical, and electrical properties which can be adjusted by the addition or substitution of various magnetic atoms (e.g., Cr, Fe, Mn). In this current study, three chalcogenide spinels (i.e., $CoCr_2S_4$, $CoCr_2Se_4$, and $CdCr_2Se_4$) were chosen as candidate materials for further investigation as radiation detection materials because of their high average atomic number (high radiation cross-section) and measured of theorized near-room temperature Curie temperatures (220–228 K (Ohgushi et al. 2008; Nolulyak et al. 1987), <212 K (Gibart et al. 1973), and 129.5 K (Baltzer et al.), respectively). Each of the three different specimens were batched separately in a nitrogen glovebox (< 0.1 ppm H_2O and O_2) using high purity ($\geq 99.99\%$) elemental chunks or powders which were loaded into a pre-cleaned¹ fused quartz ampoules. The ampoule was then sealed under vacuum ($P \sim 1 \times 10^{-5}$ Pa or 1×10^{-7} Torr) and then heat-treated in a rocking furnace at $T \geq 900^\circ C$. The specimens were then removed from

¹ Fused quartz tubes used as reaction vessels in this work were cleaned by a 2 hr RCA-1 etch (1:1:5 parts $NH_4OH:H_2O_2:H_2O$, by volume) at $70^\circ C$ followed by a 2 hr soak in acid (1:1:18 parts $HF:HNO_3:H_2O$) and then a bake-out at $1160^\circ C$ for 1 hour.

the ampoule, ground to powder in a Diamonite mortar and pestle, and analyzed with a Bruker D8 Advanced X-ray diffractometer (XRD) coupled with a LinxEye detector. Typical scan parameters were $5-110^\circ 2\theta$ at $0.015^\circ 2\theta$ steps with 0.3 second dwells per step. Jade 6, EVA, and Topas 4.2 software were used to identify and quantify phase assemblages. Samples were heat-treated, ground, and analyzed iteratively until the spinel phase achieved was $> 90\%$ of the total crystallinity of the specimen.

CoCr_2Se_4 was the first material investigated. The specimen was initially heated at 900°C for 54 hours, at which point, it was removed from the furnace. The black powder contained residual chunks of some of the original constituents (assumed to be Cr) and thus was ground in a mortar and pestle and reheated at 1000°C . X-ray diffraction confirmed two primary phases were present, CoSe and Cr_2Se_3 , with unidentified minor phases. After a second review of the literature (Barraclough 1977), it was apparent that the possibility of forming a spinel where the only chalcogen being Se might not be possible in the MCr_2Ch_4 ($\text{M} = \text{Mn, Fe, Co}$; $\text{Ch} = \text{S, Se, Te}$) system due to the instability of the spinel structure in the presence of high Z chalcogens, i.e., Se, Te. When considering $\text{MCr}_2\text{S}_{4-x}\text{Se}_x$ ($\text{M} = \text{Mn, Fe, Co}$) spinels, the spinel structure is only achievable when $0 \leq x < 2$ ($\text{M} = \text{Mn}$), $0 \leq x < 1.25$ ($\text{M} = \text{Fe}$), and $0 \leq x < 1$ ($\text{M} = \text{Co}$). Thus, the pure Se-based Co-Cr spinel was temporarily abandoned and might be revisited with a mixture of S/Se later in the project.

According to the literature (Ohgushi et al. 2008; Kalinnikov et al. 2003), it is possible to make these spinels by intimately mixing the powders of the constituents prior to heat-treatment. Hence, CoCr_2S_4 and CdCr_2Se_4 were batched from the highest purity fine powders commercially available. Each specimen was heat-treated for 30 hours at 900°C , ground with a mortar and pestle, and then analyzed by XRD for phase assemblage. Samples were heat-treated, ground, and analyzed iteratively until the spinel phase achieved was $> 90\%$ of the total crystallinity of the specimen which required 2 heat-treatments for CoCr_2S_4 and 3 for CdCr_2Se_4 . Following the first heat treatment, the CoCr_2S_4 specimen was composed of two binary materials (CoS and Cr_2S_3) and a cubic phase ($a = 9.9211 \text{ \AA}$) and after the 2nd heat-treatment, it was composed of only two phases Cr_2S_3 in addition to the cubic CoCr_2S_4 – see Table III. After each heat-treatment with the CdCr_2Se_4 specimen, it was composed of CdSe , Cr_2Se_3 , and the cubic CdCr_2Se_4 phase though the CdCr_2Se_4 phase increased dramatically with each successive heat-treatment (31.92, 75.32, and 91.89 mass% for the 1st, 2nd, and 3rd heat-treatments, respectively) – see Table IV. Figure 3-3 shows the diffraction peaks from each heat-treated specimen of CoCr_2S_4 and CdCr_2Se_4 and demonstrates the progression of spinel isolation. Magnetic properties of CoCr_2S_4 and CdCr_2Se_4 were also measured as a function of temperature (see Figure 3-4).

We had hoped to continue work on these systems, either by testing the photomagnetic effect (and comparing to effects with ionizing radiation) either at low temperatures below the Curie temperature for these materials ($< 150 \text{ K}$), or by making mixed cations including Cu to increase the Curie temperature at the expense of some metallic conductivity (Fedorov et al. 2003). However, the chalcogenide powders proved difficult to consolidate into disks that could

be used in the resonator, so future work on these materials was put on hold. We hope to publish the results we have in the future.

Table III. Summary of XRD structure data for CoCr_2S_4 sample. The ICSD# denotes the number assigned to the pattern from the International Crystal Structure Database. The Ref. denotes the reference from which the data was obtained for the structure fits. “a, b, c” denotes the unit-cell size. The size listed is the crystallite size (in nm) calculated by Rietveld refinement of the unit cells. “m%” denotes the mass% of the phase determined through analysis by Topas 4.2.

Phase (ICSD#)	Space Group	Ref.	1 st Heat Treatment			2 nd Heat Treatment		
			a, b, c	Size, nm	m%	a, b, c	Size, nm	m%
CoCr_2S_4 (43039)	Fd-3mZ	(Colominas-Broquetas et al. 1967)	9.9211, 9.9211, 9.9211	316.8	75.04	9.9241, 9.9241, 9.9241	432.7	96.64
Cr_2S_3 (16721)	R-3H	(Jellinek 1957)	5.9361, 5.9361, 16.6896	175.4	15.75	5.9345, 5.9345, 16.6542	291.1	3.36
CoS (29307)	P63/mmc	(Alsen 1925)	3.3806, 3.3806, 5.2369	31.7	9.21	-	-	-

Table IV. Summary of XRD structure data for CdCr_2Se_4 sample. β is the beta-angle in the unit cell. See Table III for a description of the other column headings.

Phase (ICSD#)	Space Group	Ref.	1 st Heat Treatment			2 nd Heat Treatment			3 rd Heat Treatment		
			a, b, c (β)	Size, nm	m%	a, b, c (β)	Size, nm	m%	a, b, c (β)	Size, nm	m%
CdCr_2Se_4 (42022)	Fd-3ms	(Riedel and Horváth 1969)	10.7465, 10.7465, 10.7465	406.1	31.92	10.7467, 10.7467, 10.7467	421.7	75.32	10.7466, 10.7466, 10.7466	444.9	91.89
Cr_2Se_3 (42704)	I12/m1	(Wehmeier et al. 1970)	6.2006, 3.6080, 11.5428 (89.60°)	100.3	38.86	6.2281, 3.5845, 11.5251 (89.24°)	267.1	17.75	6.2452, 3.6110, 11.5462 (89.98°)	155.4	5.07
CdSe (60630)	P63mc	(Stevenson and Barnea 1984)	4.3006, 4.3006, 7.0118	247.3	29.22	4.3004, 4.3004, 7.0116	146.7	6.93	4.3012, 4.3012, 7.0110	165.8	3.04

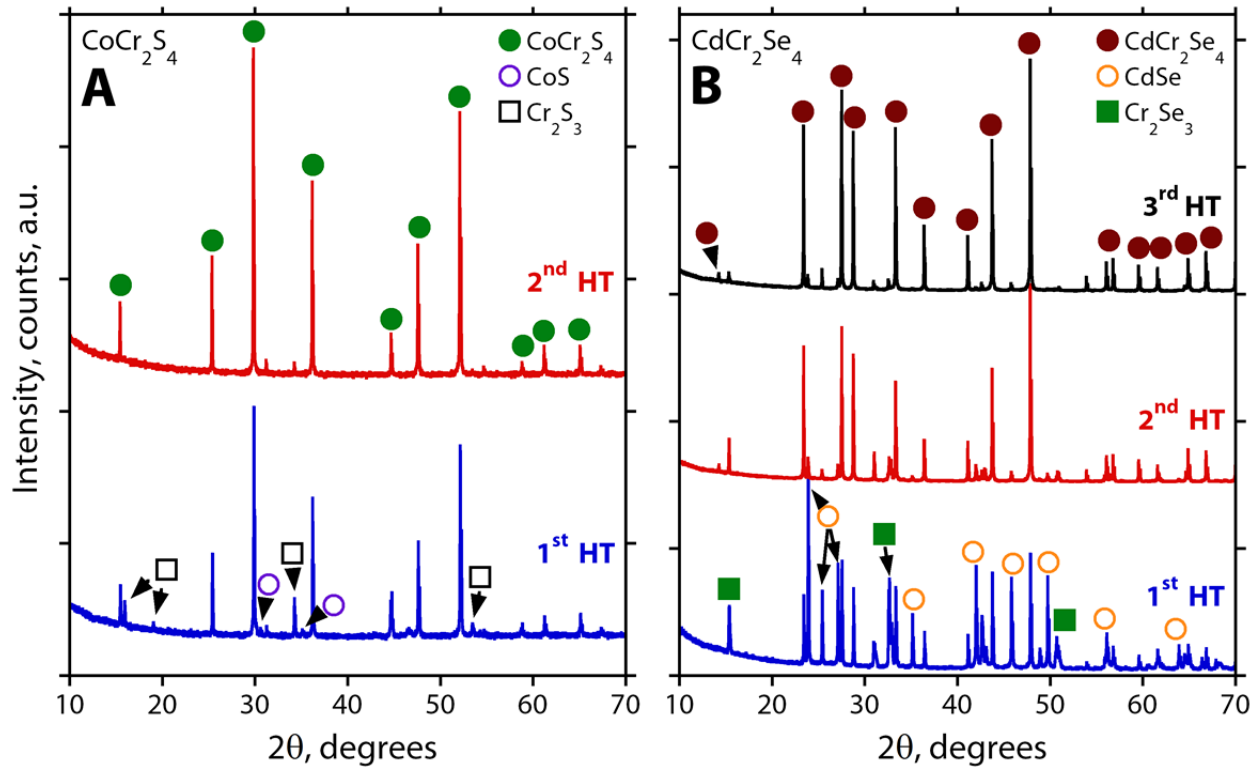


Figure 3-3: XRD spectra showing the progression of (A) CoCr_2S_4 and (B) CdCr_2Se_4 spinel production of repeated heat treatments.

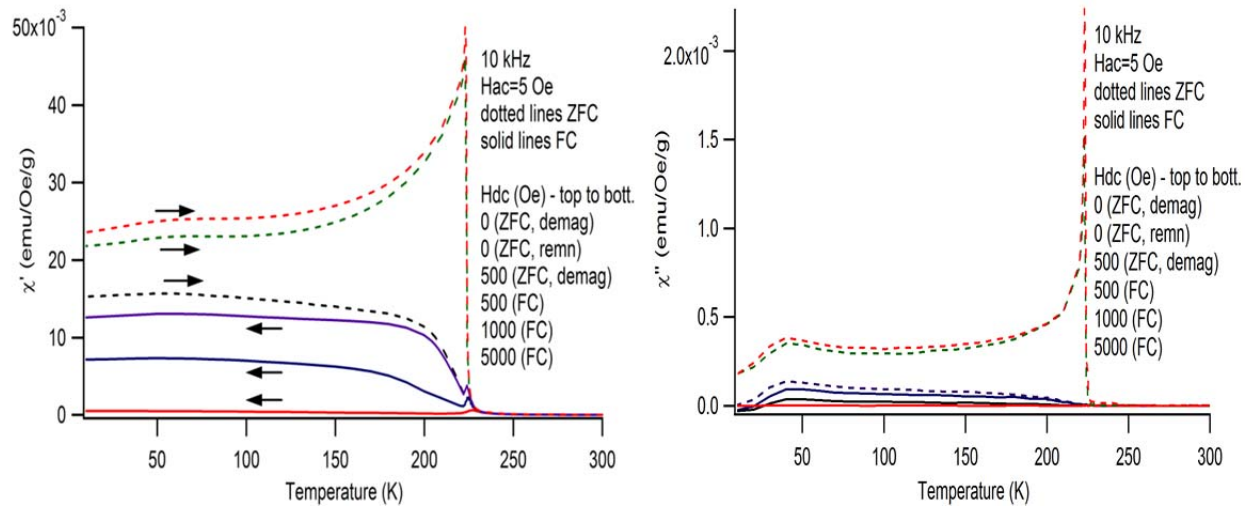


Figure 3-4: AC magnetic spectrum of CoCr_2S_4 showing real (χ') and imaginary (χ'') components as a function of various magnetic histories, field cooling (FC) under different fields, zero-field cooling (ZFC) then warming in different fields and from different starting states (demagnetized, remnant). The arrows show the direction of the measurement with temperature. The Curie temperature shows a sharp spike in both χ' and χ'' , particularly when the measurement is taken with no applied DC field.

3.1.9 Ferroelectrics

Ferroelectric relaxors such as lead magnesium niobate-lead titanate (PMN-PT) are of interest as multilayer ceramic capacitors (MLCC's) because of their low sintering temperature (as ceramics) and high peak permittivity. Additionally, their unusually high electrostriction coefficients make them attractive for electromechanical applications such as actuators. Because of their large losses in the MMW frequency range, they may also be effectively used as broadband absorbers (Kim et al. 2003). Values for DC dielectric permittivity are very high, on the order of 3000 – 8000 depending on ratio of $\text{PbMg}_{1/3}\text{Nb}_{2/3}\text{O}_3$ (PMN) to PbTiO_3 (PT). There is one report on the increase in dielectric constant with Li ion irradiation of PMN-PT (Angadi et al. 2003a). PMN-PT is very dense and has a high average atomic number (Z_{ave}) (8.9 g/cm³ and 26.9 Z_{ave} for PMN-30PT), and so should be a very efficient gamma-ray absorber.

We measured the millimeter wave properties of PMN-PT (McCloy et al. 2011b), and found that it is too absorbing at these frequencies to be useful for a stand-off detector. It may, however, be useful at lower frequencies in the microwave region, but it is still quite absorbing there as well.

LiNbO_3 and LiTaO_3 are of interest due to their wide availability and low cost as electro-optic crystals. They are available in large sizes, either as wafers or large crystals. Our split-post dielectric resonator (SPDR) measurements to date on large wafers of LiNbO_3 (MTI) gave lower than desired Q factors. We did obtain a high quality periodically poled LiTaO_3 crystal prism from Peter Dowben, University of Nebraska Lincoln, and were able to get good Q factors from the split ring resonator (SRR).

These lithium compounds have some amount of ⁶Li and could likely be enriched for better interactions with neutrons. A few recent papers have been published on ion irradiation to structure domain walls in LiNbO_3 (Jentjens et al. 2009; Zamani-Meymian et al. 2010).

3.1.10 Mica

A fairly recent paper has shown that capacitance of phlogopite mica has been shown to be highly sensitive to neutrons (cGy doses) yet insensitive to gamma rays (kGy doses) (Roy and Pandya 2005). This is probably due to its hydrogen content, as the chemical formula is about $\text{KMg}_3\text{AlSi}_3\text{O}_{10}(\text{F},\text{OH})_2$, but could also be due to lattice damage created by neutrons. Iron and sometimes manganese can substitute for magnesium leading to biotite mica, leading to the possibility of a magnetic effect also. The gamma insensitivity may be due to the low Z_{ave} and relatively low density (2.83 g/cm³). The neutron irradiation showed capacitance (permittivity) decrease showed a frequency dependence, with high frequencies (10 MHz) being the most affected. The hypothesis is that these effects would be even more pronounced at microwave frequencies, such as 8 GHz our SPDR cavity. Natural mineral mica is used in many industries, including as capacitors in electronics due to its high breakdown strength. We were able to purchase some very uniformly cleaved phlogopite mica sheets at low cost (~\$300 for 100 sheets

of 50 x 50 x 0.15 mm³) from SPI (Structure Probe, Inc., http://www.2spi.com/catalog/submat/phlogopite_mica.shtml).

Additionally, we postulated that the lithium mica known as lepidolite, with the chemical formula $KLi_2Al(Al, Si)_3O_{10}(F, OH)_2$, may also be rather neutron sensitive. This material is not available commercially but we obtained it from a mineral dealer in bulk form. It is more difficult to work with since the pieces have to be hand-cleaved and the thicknesses can be somewhat irregular, leading to problems in the resonant cavity. However, we plan to undertake some irradiation experiments with both these materials (see Figure 3-5) since they are very abundant, low cost, and in the case of phlogopite, already commercially available in the electronics industry.

We were able to test both of these mica materials in the split post dielectric resonator (SPDR). These tests included static tests and tests with feedback. We also tested with and without irradiation (see below).



Figure 3-5: Mica samples: phlogopite (left) and lepidolite (right)

3.2 Resonators

Below we discuss the other main part of this DTRA program, the simulation, design, fabrication, and measurements of the resonator. While the material part of the system is the detector element which responds to the radiation, the resonator is the read-out of the electromagnetic changes induced. Since this portion of the project has not yet been published in the open literature, more detail is provided to document the work accomplished on this project.

3.2.1 Electromagnetic modeling of resonators and materials

A series of parametric simulations was performed using Ansoft High Frequency Structure Simulator (HFSS) in order to investigate the behavior of split ring resonators (SRR) under various dielectric and magnetic loading conditions. Ansoft HFSS is an industry-standard, three-dimensional, full-wave electromagnetic field solver based on the finite element method. Constructing HFSS models generally consists of creating the geometry of interest, assigning material properties to all objects, and applying boundary conditions appropriate for the electromagnetic solution. Once the model is ready to solve, parametric sweeps can be performed in order to study relationships between variables such as geometrical features or material

properties and the electromagnetic performance of the structure. For this study, the performance parameters of interest are the resonant frequency and quality factor of the resonant cavity.

Two different solution techniques were used to predict the resonator performance. The first method is known as the eigenmode solver technique and provides the natural resonances of a given structure. In this technique, no excitation is needed and the outputs are the complex resonant frequency, unloaded quality factor, and electromagnetic field distributions of the resonant structure. The limitation of this technique in HFSS is that the design cannot include ferrite materials with a constant bias field. The second method is known as the driven modal solution and provides the frequency response of a given structure. For this solution type, an excitation must be defined to allow scattering parameters to be calculated across the frequency band (in addition to the electromagnetic field distribution). The loaded quality factor can be calculated from the scattering parameters using the full-width half-maximum value. This method does not have any material type limitations in HFSS. For the split ring resonator, the excitation is defined as an input port on a coaxial transmission line which uses a coupling loop to inductively transfer power to the resonator structure.

3.2.1.1 Model Validation using Dielectric-Loaded Cylindrical Resonator

In order to validate the modeling approach, the split-ring resonator from a publication by Kelly et al. (Kelly and Gallagher 1987) was analyzed using HFSS. This cylindrical resonator, shown in Figure 3-6, is dielectric-loaded using a LiTaO_3 crystal with a dielectric constant of 43 and dielectric loss tangent of 0.0005. Excellent agreement was obtained between the published measurements and our predictions. The SRR resonant frequency was reported in (Kelly and Gallagher 1987) to be near 860 MHz. The predicted resonant frequency was 858 MHz using the HFSS eigenmode solver and 865 MHz using the HFSS driven modal solver. The computational runtimes for these models were less than 2 minutes. The electromagnetic field distributions were consistent with expectations, showing high electric field concentrations inside the gap region loaded with the crystal.

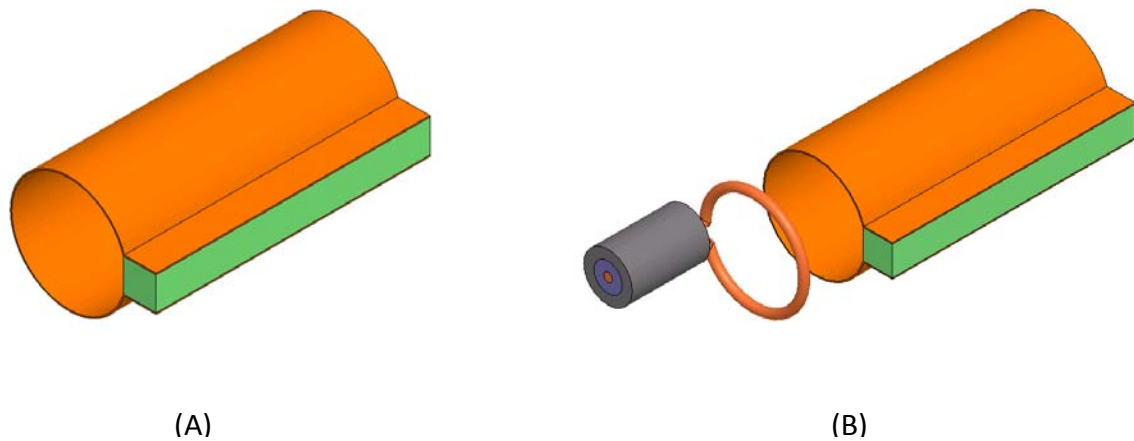


Figure 3-6: HFSS model of cylindrical split-ring resonator in reference (Kelly and Gallagher 1987). (A) Eigenmode solver (B) Driven modal solver

The results showed that HFSS could be used to efficiently evaluate the impact of material properties, geometrical dimensions, and coupling configurations on resonator performance. Parametric simulations using the eigenmode solver were then performed to establish sensitivities to dielectric constant and loss tangent for this particular resonator configuration. These results are shown in Figure 3-7. It was found that the resonant frequency varied from 845 MHz to 882 MHz for the range of crystal dielectric constants from 41 to 45, and the unloaded quality factor varied from 700 to 1700 for the range of crystal dielectric loss tangents from 0.0001 to 0.001.

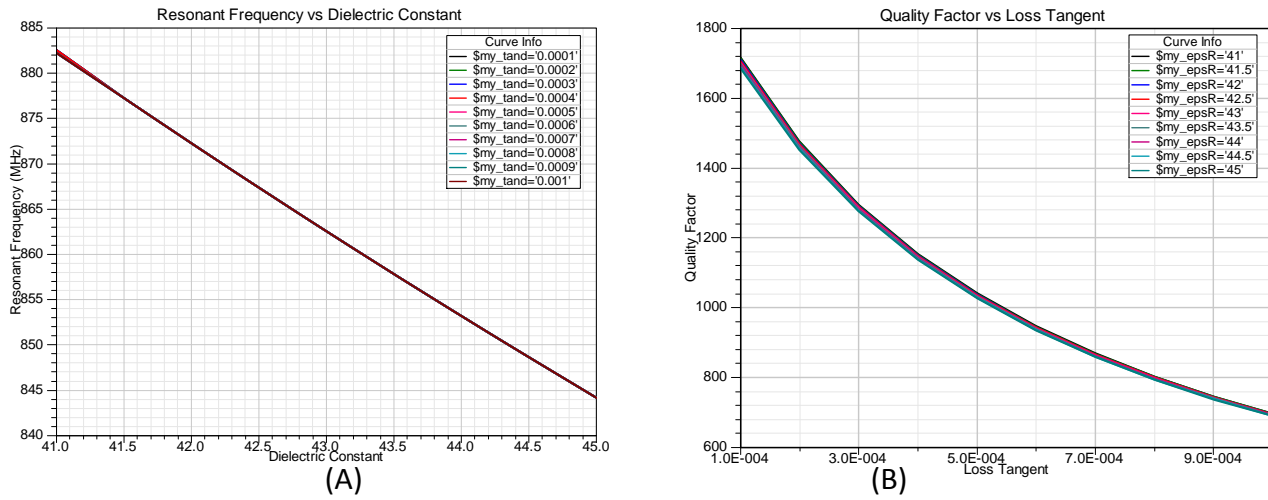


Figure 3-7: Results of HFSS model of cylindrical split-ring resonator with dielectric loading. (A) Resonant frequency versus dielectric constant (B) Unloaded quality factor versus dielectric loss tangent

3.2.1.2 Model Validation using Dielectric-Loaded Rectangular Resonator

A secondary validation of HFSS was performed for the rectangular split-ring resonator published by Young et al. in (Young et al. 2003). The eigenmode solver model of this cavity is shown in Figure 3-8. This design uses a CdSe crystal with a dielectric constant of 10 and dielectric loss tangent of 0.001. The cavity is located within a shielding box on a dielectric shim layer which provides a thermal shunt for power dissipation to the outer enclosure. As shown in Figure 3-9, the HFSS predictions agree well with published results for parametric sweeps of the shim thickness. Similar agreement was obtained for variations in the shim dielectric constant value.

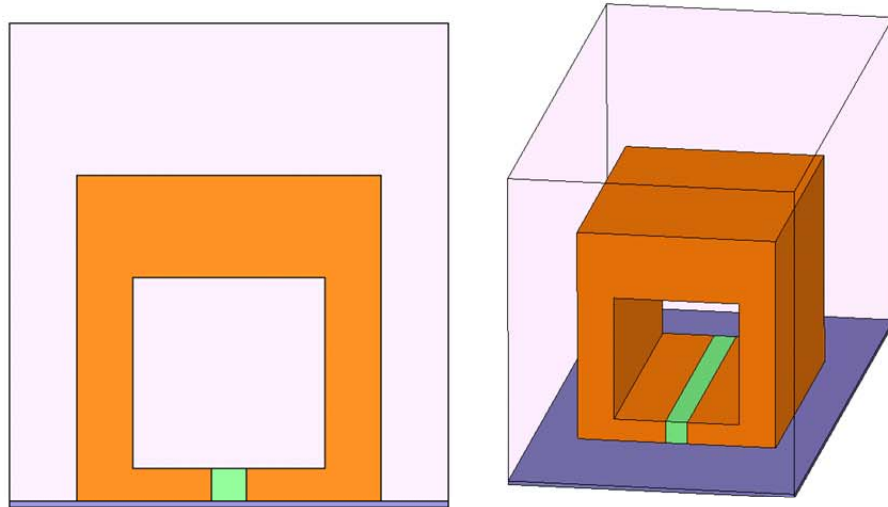


Figure 3-8: HFSS model of rectangular split-ring resonator in reference (Young et al. 2003). The design incorporates a dielectric shim for thermal management.

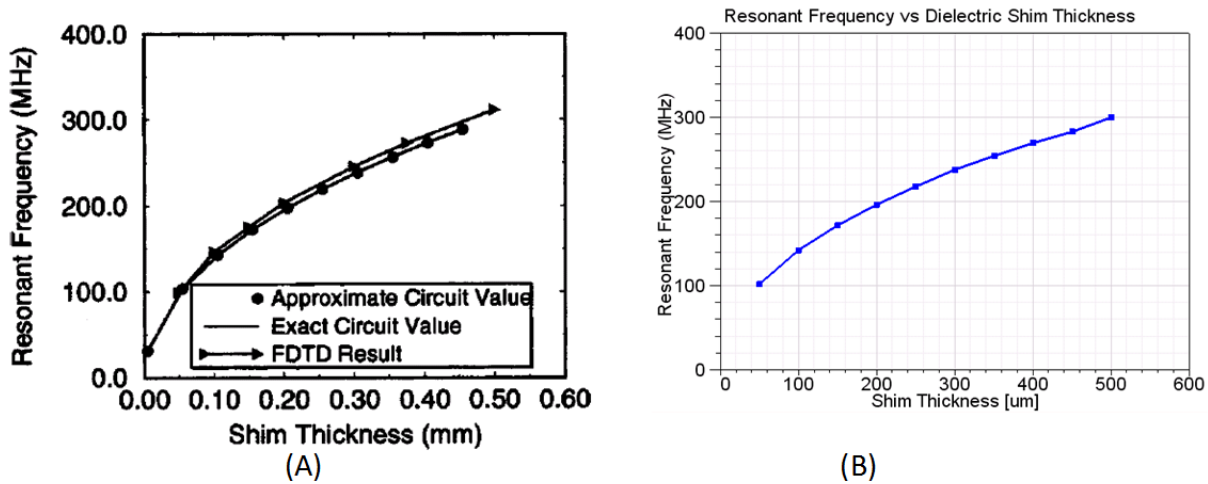


Figure 3-9: Example comparison of published results and HFSS predictions for rectangular split-ring resonator with dielectric loading. (A) Published data (B) HFSS predictions

3.2.1.3 Resonator Bore Shape

The effect of resonator bore shape was investigated using HFSS for the designs in (Kelly and Gallagher 1987) and (Young et al. 2003). Split-ring resonator models were created having equivalent square and circular bore cross-section areas in order to determine if the uniformity and distribution of the electric and magnetic fields were significantly affected. Driven modal solutions were used with coaxial transmission lines feeding the resonator through a coupling loop. It was found that resonant frequencies agreed within 0.3% - 1% for equivalent area models, and that there were no significant differences in the field distributions inside the resonators.

These results indicated that either material shape could be used for study, depending upon availability and/or machining cost.

3.2.1.4 Feed Loop Location

The precise location of the feed loop which couples electromagnetic energy into the resonator is known to be an important factor in the frequency response. Positioning the loop requires careful manipulation to obtain stable, highly-resonant behavior from the device. An electromagnetic model was used to identify impedance trends related to the feed loop offset along the bore axis as well as in the vertical direction away from the gap. The rectangular cavity design in (Young et al. 2003) was used for this study.

It was determined that moving the feed loop towards the resonator along the bore axis reduces the impedance for a nominal loop position with no vertical offset. Feed loop locations relatively far from the resonator require a vertical offset to adjust the impedance needed for sufficient coupling. It was found that an optimum location exists along the bore axis for which no vertical offset is required to obtain a well-matched resonance for the coupling loop and resonator. Positioning the feed loop very near the resonator along the bore axis was found to also require a vertical offset away from the gap location to improve the resonant response. These types of studies are valuable for understanding complex relationships between variables in the resonator design space.

3.2.1.5 Resonator with Integrated Radiating Element

For standoff detection and remote interrogation, it is desirable to incorporate a radiating element (antenna) into the resonator design. Electromagnetic simulation was used to briefly investigate the effects of directly coupling the resonator cavity to various types of antenna elements. The HFSS driven modal solution for the design in (Young et al. 2003) was used for this study. It is known that a fundamental trade-off in antenna design exists between antenna size and radiating efficiency. As the radiating element decreases in size, the radiating efficiency decreases as well. The split-ring resonator is extremely small in terms of electrical wavelength, and it is desired that antennas which are coupled to the structure are as electrically small as feasible.

As a proof of concept, the first antenna that was coupled to the resonator was a Vivaldi (exponentially tapered-slot) element which was 0.5 wavelengths wide and 0.7 wavelengths long. This element is electrically large enough to produce desirable radiating characteristics. This configuration is shown in Figure 3-10. The coupling slot between the resonator and the antenna extended the length and width of the crystal located in the gap. No intensive effort was placed in the design of the Vivaldi element. The feed loop location was tuned for a good impedance match to 50 Ohms at the input of the coax feedline. Figure 3-11 shows the predicted return loss and field distribution for this configuration. The loaded quality factor was calculated from the FWHM frequency response to have a value of 137. The antenna exhibited a well-behaved,

directional radiation pattern with 3.7 dBi peak gain. The electromagnetic simulation showed that the highest field values were located between the shim and the cavity walls and that the radiation efficiency of the antenna was 87%. These results indicate that the resonator/antenna combination is feasible.

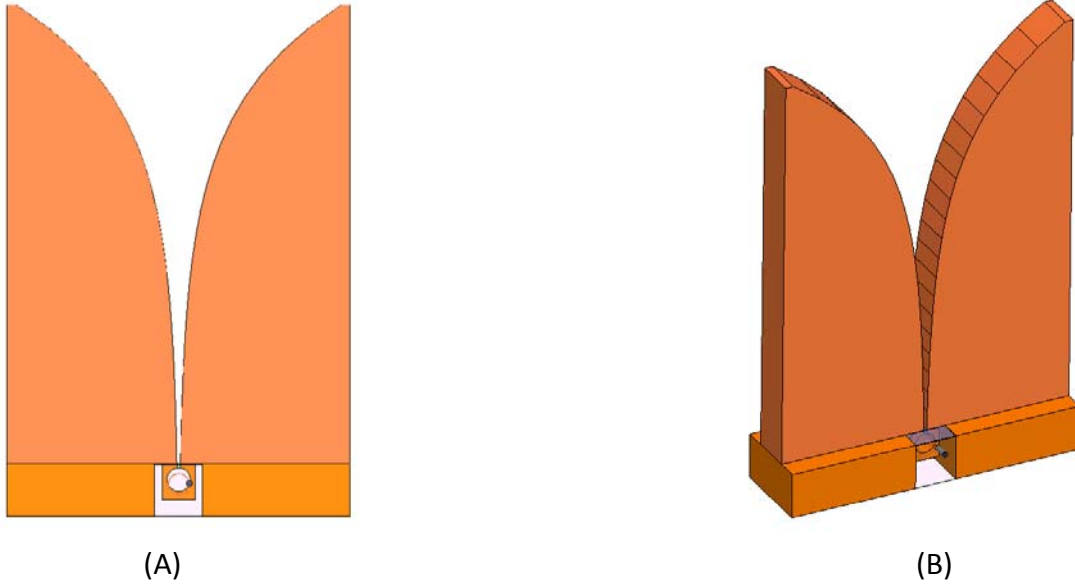


Figure 3-10: Views of HFSS model of rectangular SRR coupled to Vivaldi antenna.

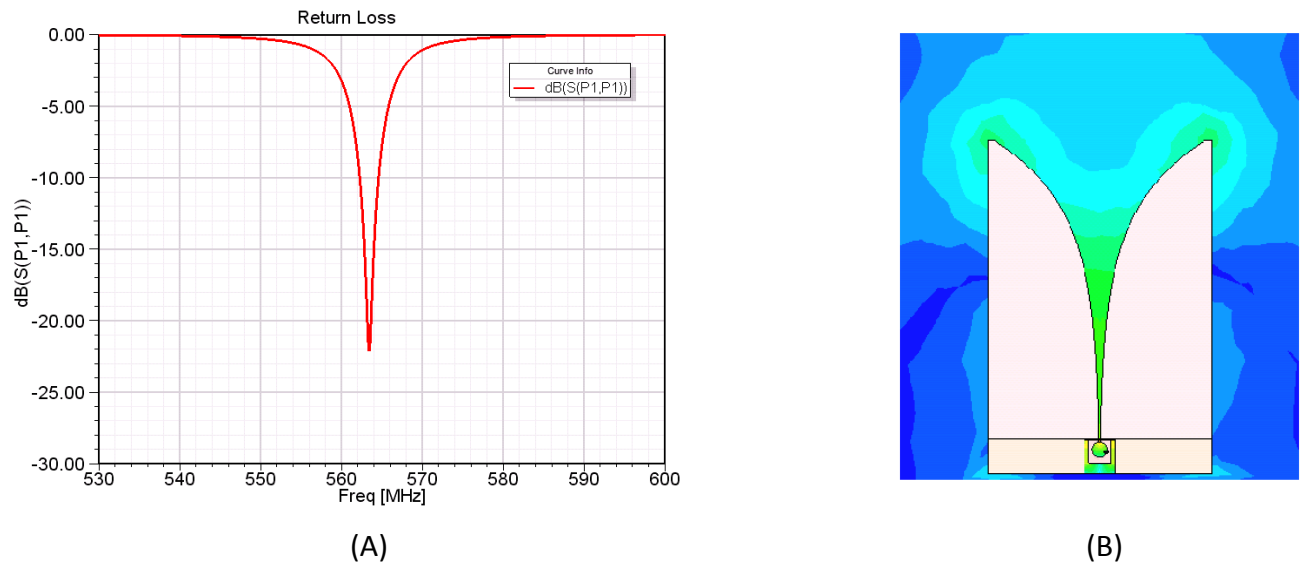


Figure 3-11: Results of HFSS model of rectangular SRR coupled to Vivaldi antenna. (A) Return loss (B) Electric field distribution

In order to reduce the size of the radiating element, the Vivaldi element was replaced with a dielectric-loaded TEM horn antenna. This configuration is shown in Figure 3-12. Increasing the dielectric constant through a loading material is a method for increasing electrical size but not physical size. A dielectric constant of 10 was used for the wedge material in the TEM horn antenna. The TEM horn antenna has electrically conducting walls on the broad side of the dielectric wedge which flare linearly along the length of the antenna. The horn length is 70 mm and width is 40 mm. The feed loop location was tuned for a good impedance match at the input of the coaxial transmission line. Figure 3-13 shows the predicted return loss and field distribution for this configuration. The loaded quality factor was calculated from the FWHM frequency response to have a value of 250. The antenna exhibited a well-behaved, broad-beamed radiation pattern with 0.7 dBi peak gain. The radiation efficiency was calculated from the ratio of radiated power to input power to have a value of 77%. Design studies showed that removing the dielectric loading material reduced the radiation efficiency to single digits. This variation demonstrates the importance of the dielectric wedge. It was also found that decreasing the dimensions of the antenna significantly reduced the radiation efficiency to values near 20%. These studies showed that the design of an unobtrusive, physically small, well-performing resonator and radiator combination may be a challenging endeavor.

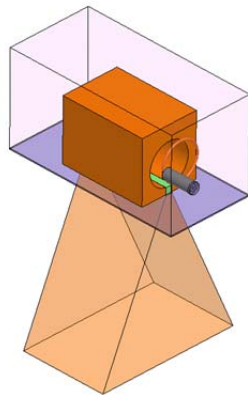


Figure 3-12: View of HFSS model of rectangular SRR coupled to dielectric-loaded TEM horn antenna.

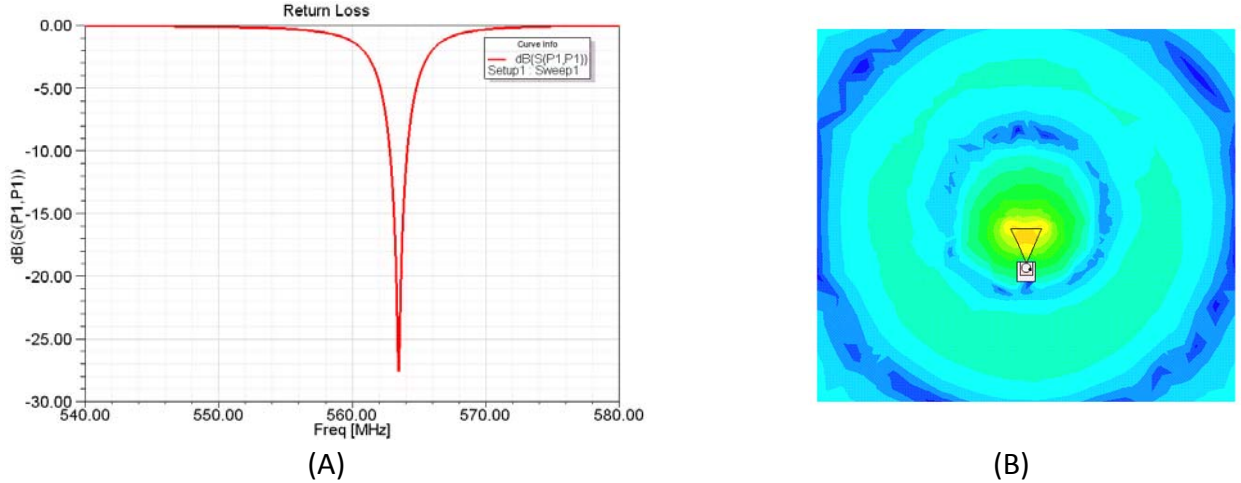


Figure 3-13: Results of HFSS model of rectangular SRR coupled to TEM horn antenna. (A) Return loss (B) Electric field distribution

3.2.1.6 Magnetic-Loaded Split-Ring Resonator

An electromagnetic model was created for a cylindrical split-ring resonator available for experimental testing in this study. This model is shown in Figure 3-14. The behavior of the resonator was modeled while loaded with barium hexaferrite. A driven modal solution was used to model the frequency response for a given uniform bias field along the bore axis. The ferrite properties used in the model are a dielectric constant of 15, relative permeability of 1.18, magnetic loss tangent of 0.015, magnetic saturation of 4700 Gauss, linewidth of 323 Oersteds, and DC bias field of 20,000 Oersteds. HFSS assumes that the magnetic material is saturated. The feed loop position was varied to obtain the sharpest possible resonance. Good agreement was obtained between the results of this model and measurements performed for this resonator. The return loss comparison is shown in Figure 3-15. Agreement of the resonant frequency is within 1.6%, taking the difference between the measured and simulated normalized by the measured.

An HFSS eigenmode solver model was also generated for this resonator configuration in order to study sensitivities to material properties. No DC bias field was entered for this model. The relative permeability was varied over a range of 1.0 to 2.0 and the magnetic loss tangent was varied over a range of 0.005 to 0.03. Figure 3-16 shows the results of this study. It was found that the resonant frequency varied from 1.4 GHz to 1.75 GHz and unloaded quality factor varied from 50 to 275 for these changes in material properties.

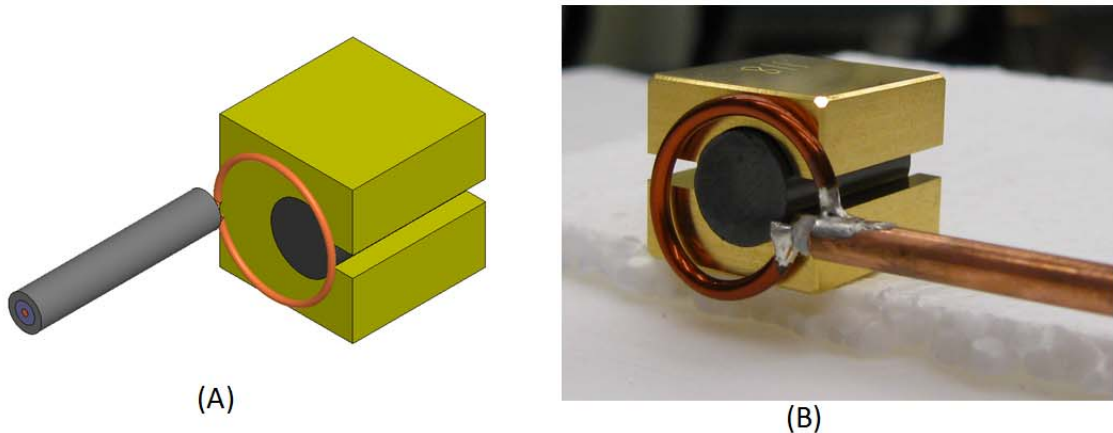


Figure 3-14: Cylindrical SRR with Barium Hexaferrite magnetic loading. (A) View of HFSS model (B) Actual resonator and inductive coil.

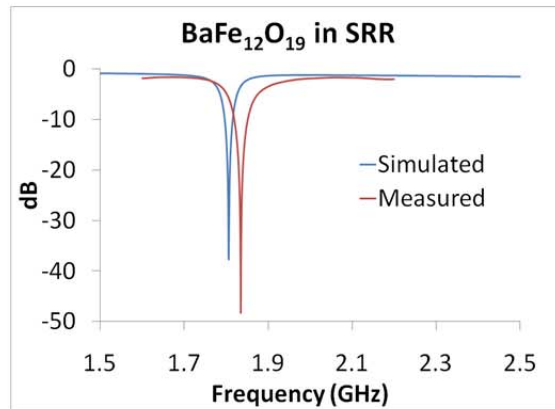


Figure 3-15: Comparison of HFSS prediction & measurement for return loss of magnetic-loaded SRR.

3.2.1.7 Dielectric-Loaded Split-Ring Resonator

The model of the resonator geometry shown in Figure 3-14 was modified to study dielectric loading. This was performed since a single resonator geometry was desired for studying both the effects of magnetic and dielectric loading. A LiTaO₃ crystal was used in the gap with a nominal dielectric constant of 43 and dielectric loss tangent of 0.0005. The dielectric constant was varied over a range of 41 to 45 and the dielectric loss tangent was varied over a range of 0.0001 to 0.001. It was found that the resonant frequency varied from 935 MHz to 978 MHz and unloaded quality factor varied from 550 to 1050 for these changes in material properties. A comparison of the magnetic and dielectric loaded SRR parametric studies is shown in Figure 3-16.

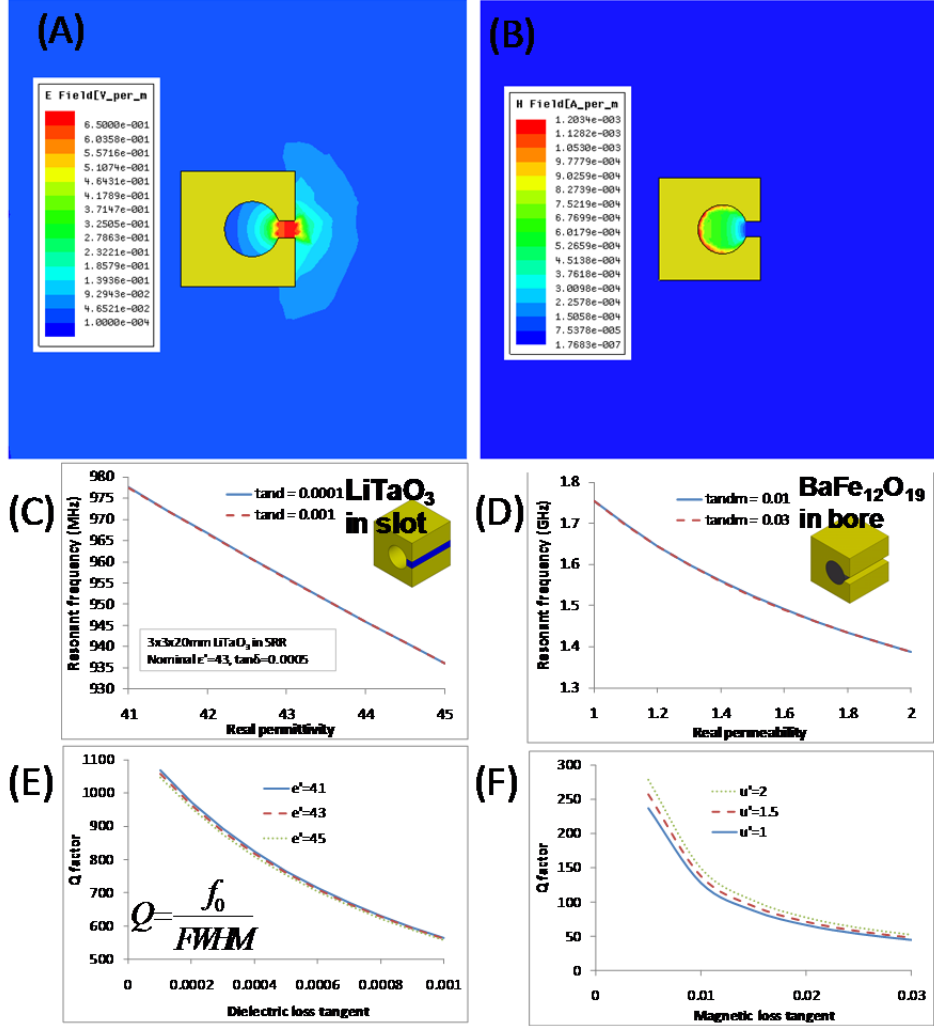


Figure 3-16: Summary of direct comparison of parametric eigenmode simulations of the same SRR loaded with ferroelectric (left column) or magnetic (right column) materials. (A) and (B) show simulations of the confinement of the electric or magnetic fields, respectively. (C) and (D) show the change in resonant frequency as a function of permittivity or permeability, respectively. (E) and (F) show the Q factors as a function of dielectric or magnetic loss tangent, respectively.

3.2.1.8 Summary

It was found that electromagnetic modeling was very useful for this study. The accuracy of HFSS was validated using published resonator configurations, and good agreement was also obtained for a magnetic-loaded resonator configuration tested during this study. This capability was used for a variety of investigations which increased the understanding of resonator operation. In particular, sensitivity studies are very useful to calibrate expectations for the relationships between resonator characteristics and changes in the electromagnetic properties of the loading materials.

3.2.2 Static resonant cavity measurements

Measurements were performed using three different cavities. Two were commercial cavities (QWED, Warsaw, Poland, <http://www.qwed.com.pl/resonators.html>) purchased on a related NA-22 project: the split post dielectric resonator (SPDR) and the dielectric ring resonator (DRR). The SPDR measures permittivity of thin, flat samples. The DRR measures permeability of small cylinders. The third cavity tested was a custom split ring resonator (SRR) constructed for a previous project involved electro-optical modulation of laser light. The advantage of the SRR is that it allows relatively large volumes of either dielectric/ferroelectric materials or magnetic materials to be incorporated into the resonant structure. The SRR as currently designed is inductively coupled, either at one end for a reflection measurement (S_{11}) or at both ends for a transmission measurement (S_{12}). See Table V for characteristics of the cavities, Table VI for their dimensions, and Figure 3-17 for photographs of the resonant cavities.

A number of materials were measured using the various cavities. Details of these measurements are shown in Table VII. Based on our experience with these cavities, we can conclude the following about their sensitivity and repeatability. The DRR can measure real (μ') and imaginary (μ'') permeability, $\mu' \pm 0.003$ or better, $\mu'' \pm 0.0003$ or better. The SPDR can measure real (ϵ') and imaginary (ϵ'') permittivity, $\epsilon' \pm 0.05$ or better, $\epsilon'' \pm 0.0005$ or better. Repeatability measurements on 7 high resistivity (2" diameter wafers, intrinsic undoped float zone Si, $[111] \pm 0.05^\circ$ orientation, polished on both sides, $4000 - 5000 \Omega\text{-cm}$, 280 μm thick) silicon wafers indicated that the error (as defined by the mean divided by the standard deviation) was 0.05-0.32% on the dielectric constant (ϵ' or permittivity) and 1.8-7.8% on the loss tangent ($\tan \delta = \epsilon''/\epsilon'$).

It was discovered early on that materials which were too lossy did not allow sufficient cavity Q for useful resonator measurements. In the SPDR, Si wafers with higher conductivity (0 – 100 Ωcm resistivity, 660-737 μm thick) highly attenuated the cavity Q and did not resonate at all. Likewise, when lithium niobate wafers were tested in the SPDR, the main 8 GHz resonance was not present, but some higher harmonics were visible with reasonable Q. It is not known at this time whether this effect was due to ferroelectric domain boundaries in the 2" wafer, off stoichiometry (this LiNbO_3 was “congruently melting” which is the more inexpensive commercial form, not “stoichiometric”), crystal miscut, birefringence, or some other effects. When the yttrium iron garnet ($\text{Y}_3\text{Fe}_5\text{O}_{12}$, YIG) cylinders were tested in the large SRR, the resonant frequency was very low, <0.5 GHz, and the Q factor was also very low ~5. This effect is believed to be due to so-called low field losses, since the polycrystalline, multi-domain ceramic has randomly oriented magnetic moments in the demagnetized case (Krupka and Geyer 1996). YIG is a very soft magnet, so it can be poled with a small hand magnet. When this was performed, the Q did in fact improve and the resonant frequency shifted. This problem persisted in the other CVG YIG (calcium vanadium garnet, which is Ca and V doped YIG (Cruickshank 2003)) measured in the SRR.

However, when measurements of these same YIG and CVG materials were made in the DRR, which is above the spin resonance frequency of about 5 GHz, losses were very minimum and Q's were very high as shown in Table VII. For these latter DRR measurements of the soft magnets, placement of a permanent hand magnet near the resonator resulted in a lowering of the resonant frequency due to an increase in permeability bringing the real permeability closer to one (see Figure 2.3 previously discussed).

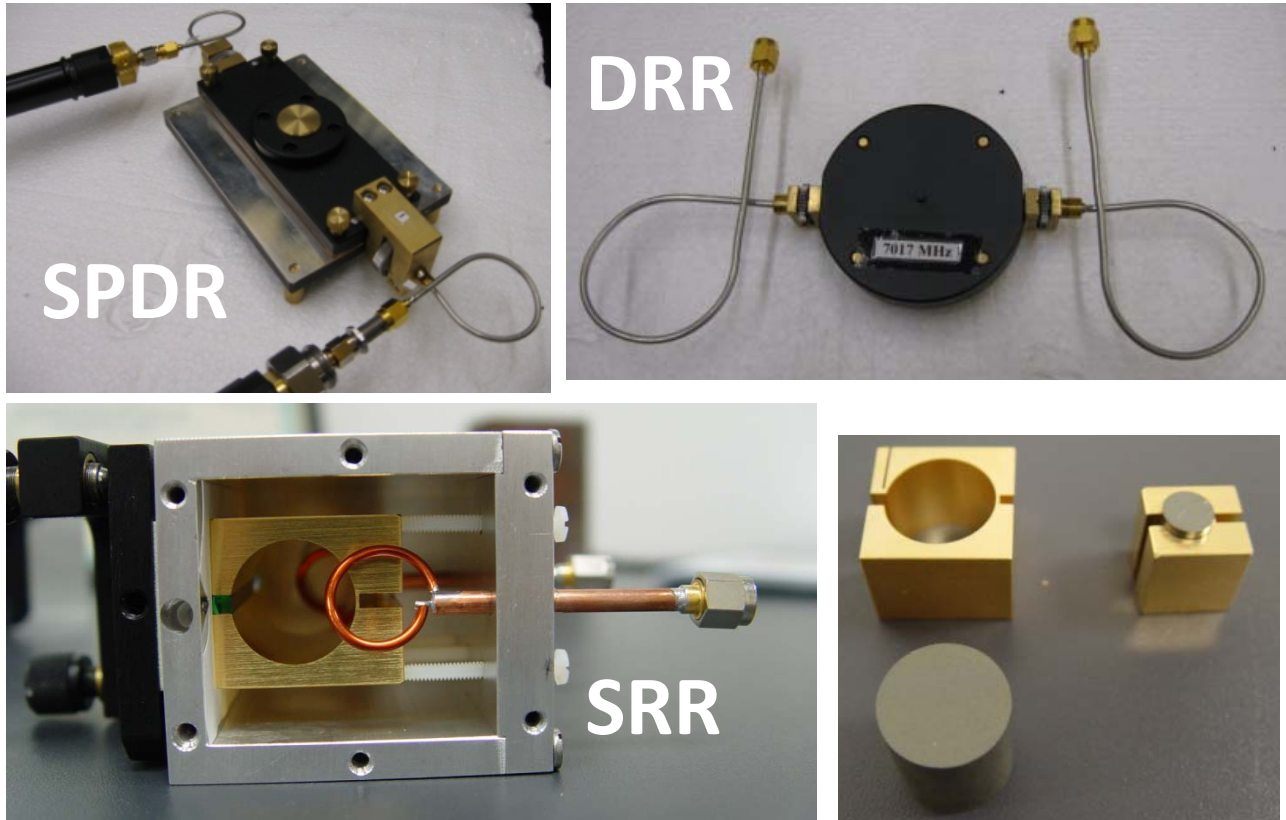


Figure 3-17: Resonant cavities tested. Note the two sizes of the SRR cavities (dimensions in Table VI)

Table V: Resonant cavity characteristics

Cavity	Resonant frequency (GHz)	ϵ	μ	Materials tested
SRR-L	0.2 - 0.5	Yes	Yes (hard ferrites)	YIG, CVG YIG
SRR-S	0.1 - 1.9	Yes	Yes (hard ferrites)	YIG, CVG YIG, Ba-M hexaferrite
SPDR	8	Yes	Only with magnetic field	LiNbO_3 , high resistivity Si, films on Si, phlogopite mica, lepidolite mica, YIG
DRR (H_{011})	6 - 8	No	Yes	YIG, CVG YIG

Table VI: Resonant cavity dimensions

Cavity	SRR length (mm)	Bore diameter (mm)	Slot width (mm)	Slot depth (mm)	Material volume mm^3
SRR-L	20	20.57	3	3	180 (slot) 6446 (bore)
SRR-S	20	9.6	3	3	180 (slot) 1448 (bore)
SPDR		6.5	0.9		30
DRR (H_{011})	9	2			28

Table VII: Material measurements using resonant cavities

Cavity	Materials tested	f_r (GHz)	Q	ϵ'	μ'
SRR-L	$Y_3Fe_5O_{12}$	0.4875	5.6	15 (assumed)	1.9
	$BaFe_{12}O_{19}$	1.6-2.1	70-88	15 (assumed)	1.18
SPDR (8.20 GHz)	Empty	8.1964-8.1967	6950-6960		
	$LiNbO_3$	11.084-11.212	175-200		
H_{011} (7.85 GHz)	Si (high resistivity)	8.016-8.018	1505-2555	11.63-11.77	N/A
	PZT on Si	8.0145	2300	30.9-36.5 (film)	N/A
H_{011} (7.85 GHz)	$BaTiO_3$ on Si	8.0161	2250-2255	21.3-27.5 (film)	N/A
	Mica, phlogopite	8.147-8.155	5600-5800	5.61-6.51	N/A
H_{011} (7.85 GHz)	Mica, lepidolite	8.015-8.018	5630-5720	5.81-5.89	N/A
	$Y_3Fe_5O_{12}$	7.795-7.796	4190-4220		
H_{011} (7.85 GHz)	Empty	7.8516	5200-5300		
	$Y_3Fe_5O_{12}$ (demag)	7.929-7.932	4300-4400	N/A	0.808
	$Y_3Fe_5O_{12}$ (saturated)	7.832-7.833	3700-3800	N/A	0.997
	CVG YIG (demag)	7.902 – 7.906	4300-4600	N/A	0.851-0.859
	CVG YIG (saturated)	7.838 – 7.842	4000-4200	N/A	0.977-0.985

3.2.3 Design, construction, and testing of GEN-1 feedback amplifier

In the course of this program we designed, built, and tested two generations of feedback amplifier designs. The first generation design, denoted “GEN-1,” is described in this section. The second generation design, denoted “GEN-2,” is described in the following section.

In order to detect transient changes in material properties which are due to induced radiation effects, a microwave circuit was constructed which employs regenerative (positive) feedback to monitor the material-filled resonator structure for slight changes in resonant frequency. The schematic block diagram of this design is shown in Figure 3-18 and the implemented circuit is shown in Figure 3-19. The circuit was constructed using discrete coaxial connectorized components to permit changes to the design as needed and to reduce costs. The circuit design can be considered to consist of two functional blocks, one which generates an oscillating signal at the resonant frequency of the material-filled resonator and one which down-

converts this signal for display using a digital oscilloscope. The two functional blocks correspond to the two separate plates upon which the design was constructed. During radiation dosing experiments, a sealed source will be placed near the material-filled resonator and the down-conversion plate and all associated RF equipment will be located several feet away from the source. Figure 3-20 illustrates the arrangement that was used during the initial irradiation experiments.

A regenerative circuit employs positive feedback between the input and output of an amplifier to significantly increase the signal strength. Positive feedback occurs when the phase of the feedback signal is in phase with the input signal and thus reinforces the signal strength. The addition of a resonator to the feedback loop serves to filter the signal so that only the frequency of the resonator is amplified. This type of circuit is well-known and was patented by Edwin Armstrong in 1914 for use as a high-sensitivity radio receiver (Armstrong 1914, 1917). Increases of 1,000 to 100,000 times for the gain and the passive quality factor (Q_{stat}) of the circuit are achievable due to the positive feedback (ARRL 1978). The Q factor is a measure of the frequency selectivity of a resonant circuit and is defined as $f_0 / \Delta f$, where f_0 is the center frequency and Δf is the bandwidth between the -3 dB frequencies (Baker-Jarvis et al. 2001). Regenerative circuits with dielectric resonators in the feedback loop have been used to construct low phase noise microwave oscillators (Taber and Flory 1995; Ishihara et al. 1980).

The fast response time and continuous monitoring provided by the resonant feedback loop is well-suited for studying transient phenomena such as that caused by ionizing radiation. Depending upon the circuit implementation and miniaturization, the response time for tracking the resonant frequency is on the order of 10 to 100 nanoseconds. This allows for precise measurements of fast changes in electromagnetic properties that may occur due to photons, gamma rays, or neutrons interacting with the material inserted into the resonator. Any changes in the material properties will produce a corresponding change in the signal frequency in the feedback loop. Amplifying the signal directly at the resonant cavity reduces external noise sources and provides the highest signal-to-noise ratio for change detection. A sudden increase in the noise level near the resonant frequency can also be used to detect transient effects.

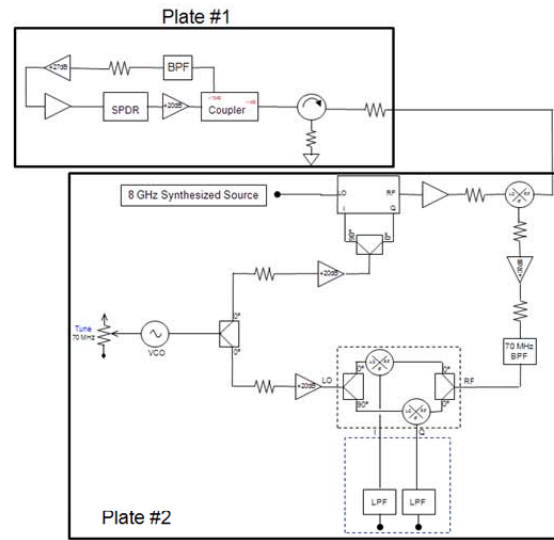


Figure 3-18: Schematic block diagram of regenerative amplifier circuit

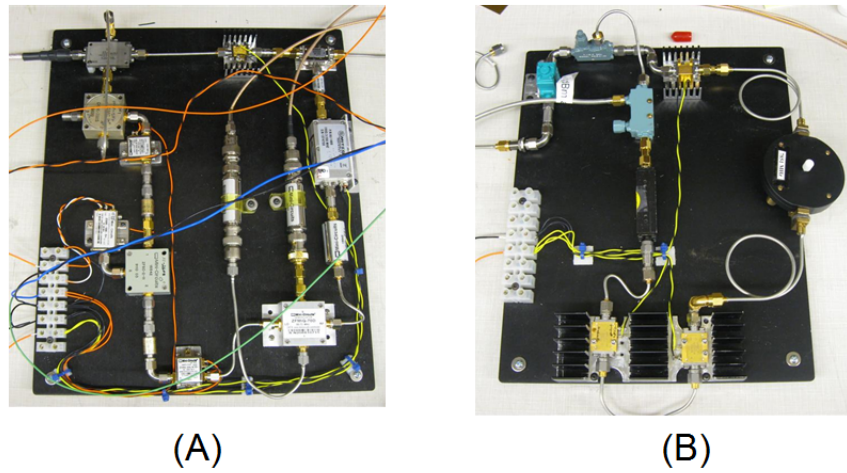


Figure 3-19: Circuit implementation of regenerative amplifier. (A) Down-conversion plate (B) Resonator plate

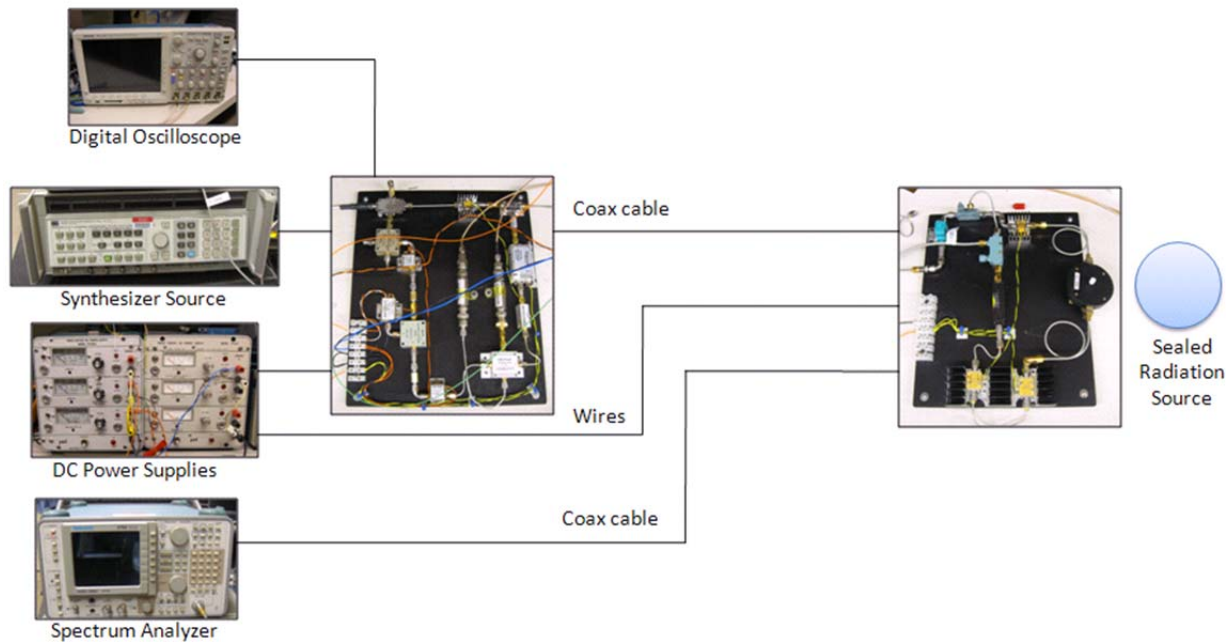


Figure 3-20: Arrangement for irradiation testing using regenerative amplifier

3.2.3.1 Resonator Feedback Loop

The resonator feedback loop is located on the resonator plate and can accommodate either of several resonant cavities which can be used to test various magnetic and dielectric materials. Initial experiments were performed using a split-post dielectric resonator which operates at 8.2 GHz and a dielectric ring resonator which operates at 7.85 GHz. The split-post dielectric resonator can be used to characterize dielectric materials and the dielectric ring resonator can be used to characterize magnetic materials. This portion of the circuit consists of several microwave amplifiers and a bandpass filter to provide positive feedback from the output to the input of the resonant cavity. The band-pass filter is located in the feedback loop to avoid spurious resonances outside the frequency band of the resonator. Any changes in the material properties will produce a corresponding change in the signal frequency in the feedback loop. This loop is also initially examined using a spectrum analyzer to ensure that a signal exists at a known frequency. A directional coupler and circulator are used to send this signal to the RF port of a mixer located on the downconversion plate.

3.2.3.2 Downconversion and Display

The superheterodyne circuit on the downconversion plate contains a quadrature-IF double-balanced mixer which uses signals from a microwave synthesizer source and a voltage-controlled oscillator (VCO) to generate a signal near the frequency of the resonant circuit. The frequency offset between the synthesizer source and the resonant circuit sets the frequency of the IQ baseband signals. The quadrature-IF mixer output signal is amplified and sent into the LO

port of a mixer connected to the resonant circuit, and the resulting 70-MHz IF output is amplified, filtered, and sent into the RF port of an IQ demodulator. The 70-MHz VCO signal is also sent into the LO port of the demodulator. The I and Q baseband signals can be monitored with a digital oscilloscope using voltage-time waveforms. Lissajous figures (Naidu 2011) can also be displayed in XY mode to track the phase differences between the two signals. The oscilloscope can be set to trigger when the waveform deviates from the nominal frequency and digitally record the waveform as it is triggered.

3.2.3.3 Radiation testing of GEN-1 feedback amplifier

The irradiation testing of resonators in the GEN-1 feedback amplifier proved to be a learning experience for the team on several fronts. The team compiled literature data on γ -ray and neutron effects on candidate materials and calculated predicted absorbed dose based on geometry, material, and energy. Four materials (see Table VIII) were tested in the presence of sealed sources of either ~ 5.7 mCi ^{137}Cs or ~ 60 μCi ^{252}Cf (total for three sources together, see Table IX). The test configuration is shown in Figure 3-21 and the individual experiments and total dosages are shown in Table X.

It was not clear, however, what the exact signature of a radiation-induced change would be in a resonator. We expected a dramatic excursion in frequency of the resonant absorption, and designed the monitoring system such that the measuring system would “trigger” when the frequency had changed by $\pm 5\%$ of the set point. We found that even without the presence of sealed sources the resonator would trigger periodically and would need to be manually reset. We attribute these excursions to thermal transients in the room and heating of the amplifiers. This was particularly evident when polyethylene moderators were used above the resonator to create thermal neutrons from the ^{252}Cf sources, as the air below the moderators and above the resonator was very hot.

A key conclusion from this round of testing was that temperature control is critical to separating any radiation-induced effects from environmentally-induced effects. Also, we wanted to be able to monitor environmental factors, such as slow long-term thermal drift, and be able to contrast them with short time scale events, such as expected from radiation interactions. To do this we had to develop a different method of data capture. In post-irradiation testing of the resonator set-up, we found that there were no apparent permanent changes in either the resonators or the materials due to the irradiation experiments.

Table VIII: Materials and resonator parameters for GEN-1 feedback amplifier sealed source testing

Material	Shape	Resonator	Q_{static}	f_{stat} (GHz)	ϵ	Supplier
Si (5000-6000 Ωcm)	0.28 mm thick	SPDR	2600	7.992	11.7	University wafer
Phlogopite mica (P-mica)	0.15 mm thick	SPDR	5500	8.140	5.6	SPI Supplies
Lepidolite mica (L-mica)	0.63 mm thick	SPDR	5830	7.991	6.8	Mineral dealer
$\text{Y}_3\text{Fe}_5\text{O}_{12}$ (YIG)	2.0 mm diameter	DRR	4300	7.932	$\mu = 0.80$	Pacific Ceramics

Table IX: Sealed sources used for GEN-1 feedback amplifier testing

Isotope	Activity	Activity date	Source #	Notes
¹³⁷ Cs	5.68 mCi	9/23/2010	318-083 (9342)	
²⁵² Cf	23.66 µCi	9/1/2008	19877 (F4-145)	Eckert and Ziegler isotope products (Burbank, CA)
²⁵² Cf	25.86 µCi	9/1/2008	(F4-146)	Eckert and Ziegler isotope products (Burbank, CA)
²⁵² Cf	10 µCi	9/15/2008	20679 (F4-712)	

Table X: GEN-1 feedback amplifier sealed source testing exposures

Sample	Date of test	Distance to source (cm)	Exposure (h:mm)	PE moderator	Notes
Si #6	9/23/2010	8	4:15 gamma	N/A	
P-mica #1	9/23/2010	11	3:46 neutron	25 cm	
L-mica #2	9/23/2010	11	2:08 neutron	25 cm	Sensitive to human proximity
L-mica #2	9/23/2010	61	1:35 neutron	75 cm	
YIG #1	9/24/2010	~200	1:59 neutron	150 cm	
YIG #1	9/24/2010	9	3:19 gamma	N/A	

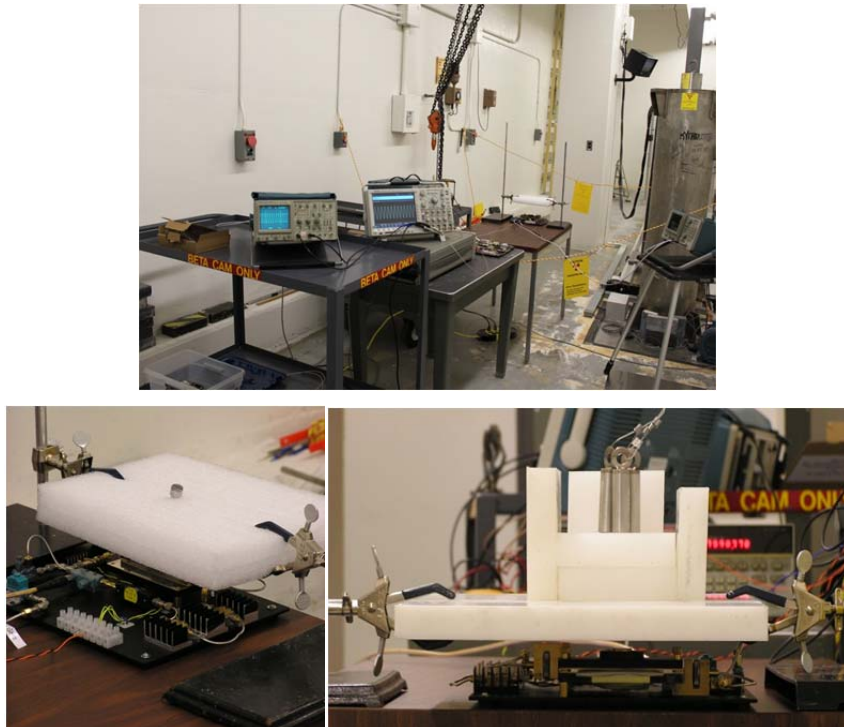


Figure 3-21: Arrangement for irradiation testing of GEN-1 system. (Top) overall experimental set-up. (Bottom, left) Cs-137 source over split-post dielectric resonator. (Bottom, right) Cf-252 sources with polyethylene moderators over dielectric ring resonator.

3.2.4 Design, construction, and testing of GEN-2 feedback amplifier

In order to incorporate the lessons learned during use of the GEN-1 resonator system, two main changes were made to the design (see Figure 3-22). First, the thermal management was significantly improved by removing the resonator from the plate containing the amplifiers. The resonator was placed on a thermo-electric cooler (TEC) and a finned heat sink. The control of temperature fluctuations on the cold plate was found to be $\pm 0.1^{\circ}\text{C}$ when the PID controller for the TEC was set for slightly below room temperature (i.e., $\sim 19.0^{\circ}\text{C}$).

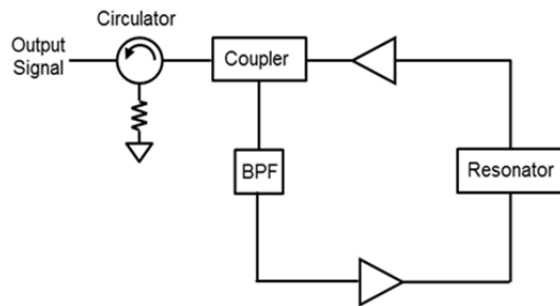
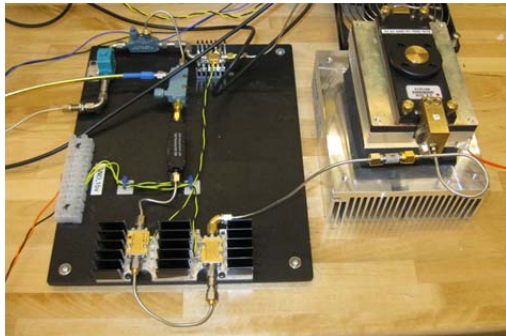


Figure 3-22: Regenerative amplifier circuit with split post dielectric resonator on thermo-electric cooler block

Second, we leased a state-of-the-art Real Time Spectrum Analyzer (RTSA, Tektronix, model # RSA-6114A). The RTSA monitors the output signal to capture disturbances due to material interactions with radiation. The RTSA can sample at 292,000 wave forms (spectral displays) per second, giving the capability to monitor 3.7 microsecond transient events. The delay in the regenerative feedback circuit is much smaller than this, on the order of 10 to 15 nanoseconds. The RTSA has a digital phosphor display which enables controllable persistence for each pixel, allowing visualization of time decay of the frequency content. Other features allow envelope capture so the furthest excursions of environmental factors such as thermal drift can easily be recorded. The output can be viewed in real-time, but the instrument can only capture one to two minutes of data (depending on bandwidth) before filling the hard drive. The system can be set to trigger on excursions of particular frequency content. Additionally, the RTSA model used in this work was able to operate at frequencies up to 14 GHz using its own internal super-heterodyne receiver, allowing direct monitoring of the ~ 8 GHz signal without an on-board down-conversion to the 1 MHz intermediate frequency (IF) as required in the GEN-1 system. This probably provided greater system stability, since the GEN-1 down-converter circuitry was co-located near the sources and their excess heat burden.

The RTSA allowed us to investigate the dynamic quality factor (Q) of the resonators in the feedback loop (see Table XI). We found that the feedback circuit produced gain narrowing of the resonator, and an enhancement over the static Q of up to 10,000. This gave dynamic Q 's for loaded resonators up to 10 million in some cases. The self phase-locked frequency also shifted

somewhat from the static (vector network analyzer) measurements of the resonator frequency due to the additional phase delay from the feedback loop components.

Table XI: GEN-2 feedback amplifier resonator parameters

Resonator	Material	f_{stat}	f_{dyn}	Q_{stat}	Q_{dyn}	Active material volume (cm ³)
SPDR	Empty	8.196	8.193	6,650	51,000,000	N/A
SPDR	Si	7.992	8.034	2,600	9,000,000	0.57*
SPDR	Li mica	7.991	8.068	5,830	4,000,000	<0.40*
DRR	Empty	7.852	7.852	5,340	68,000,000	N/A
DRR	YIG	7.932	8.528	4,400	15,000,000	0.03
SRR#1	CdTe	0.287	0.287	1,000	8,700,000	0.18
SRR#2	LiTaO ₃	1.305	1.397	180	450,000	0.18
SRR#2	YIG	1.090	1.540	10	10,000	6.65
SRR#2	CdSe	1.267	1.707	420	210,000	0.18

*note that in the SPDR, not all of the volume is “active” in the resonator, so this # is an overestimate

3.2.4.1 Split ring resonators (SRRs)

To test the effects of frequency and larger material volume (potentially better stopping power), positive feedback resonant circuits similar to that used in the GEN-2 system were constructed on aluminum plates with excellent “thermal inertia” (large thermal mass). Rather than using commercial SPDR and DRR cavities, these feedback resonators used custom split ring resonators (SRRs) designed originally for electro-optic modulation of lasers (see Figure 3-23 and Figure 3-24) (Kelly and Gallagher 1987; Young et al. 2003). The resonant frequencies of these SRRs were $\sim 0.3 - 1.3$ GHz depending on the material, which is much lower than the ~ 8 GHz for the commercial SPDR and DRR cavities (see Table XII).

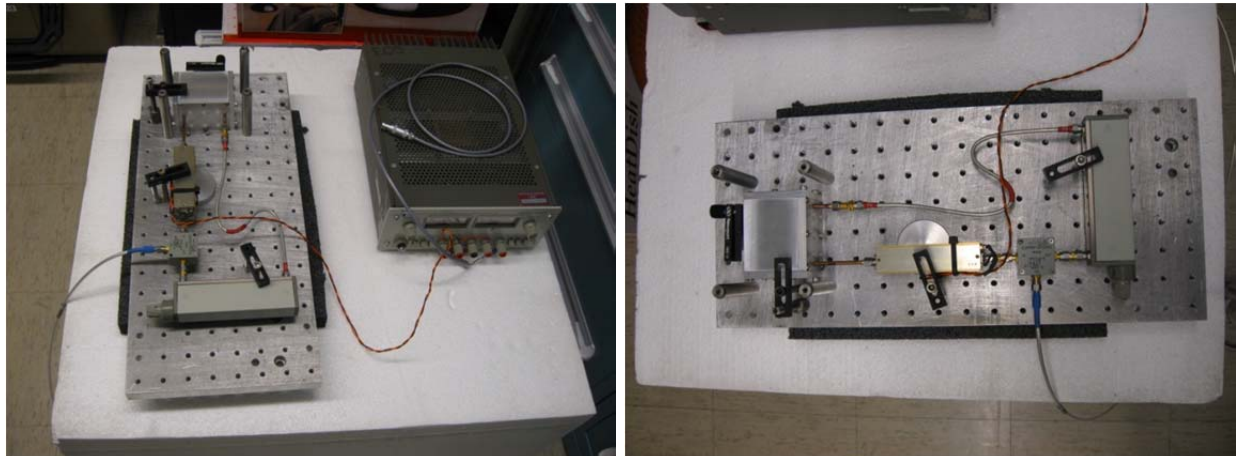


Figure 3-23: SRR#1 with closed sides. The plate contains both the resonator circuit and the SRR with CdTe inside the aluminum box.

Table XII: SRR feedback amplifier parameters

SRR Bore diameter	SRR Slot length (mm)	Active material	SRR circuit #	Notes
20.57	40	CdTe	1	Perfectly fills slot
20.57	40	LiTaO ₃ , unpoled section across gap	2	Underfills slot
20.57	20	YIG	2	Perfectly fills bore
20.57	20	LiTaO ₃ , poled section across gap	2	Overfills slot
20.57	40	CdSe	2	Perfectly fills slot

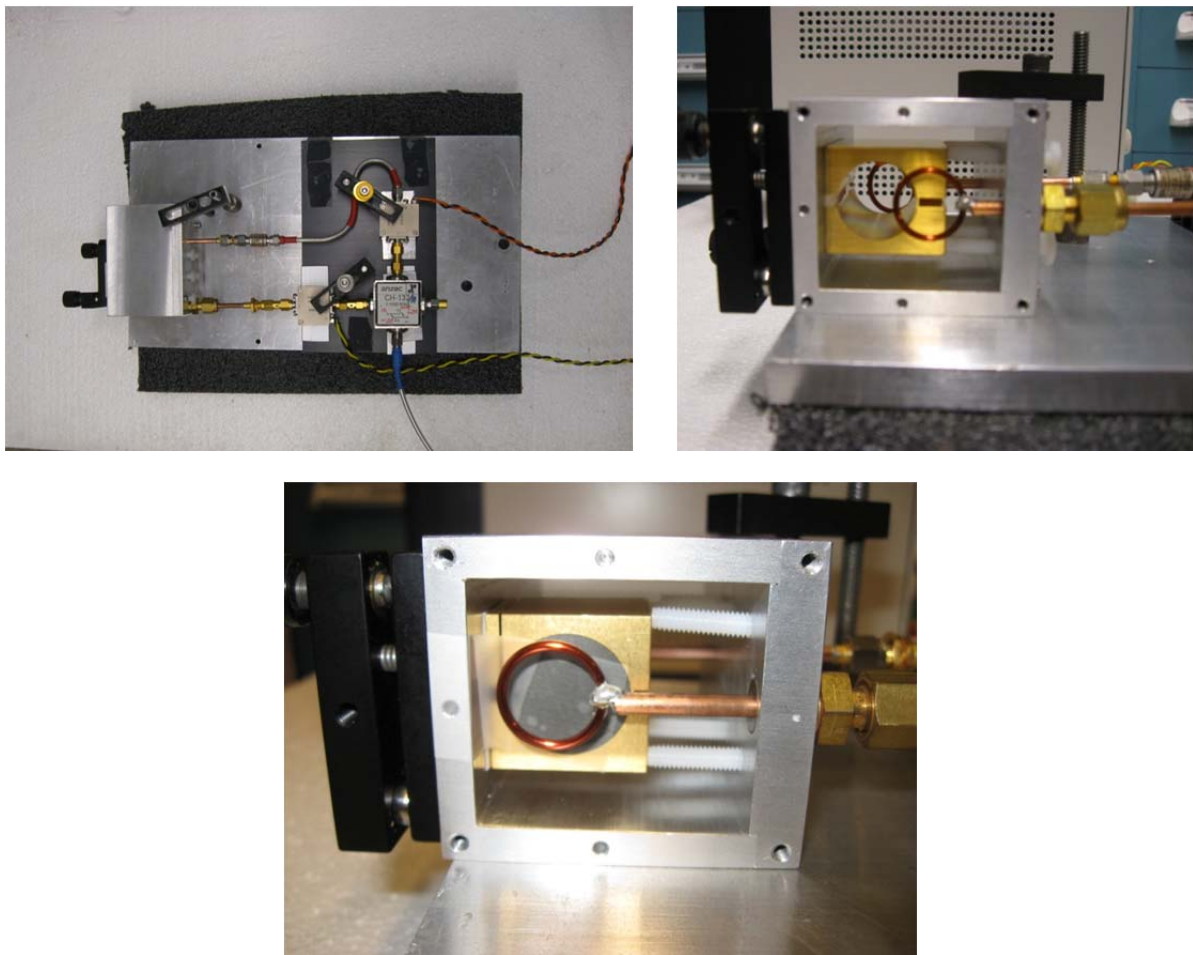


Figure 3-24: SRR#2 with open sides. The plate contains both the resonator circuit and the SRR. Shown are the SRR with periodically poled LiTaO₃ in the slot and with YIG in the bore.

3.2.4.2 Radiation testing of GEN-2 feedback amplifier and SRR

Two series of tests were performed on the GEN-2 system and the SRR systems. The first involved testing in the PNNL Engineering Development Laboratory (EDL) where we explored many different configurations, assessed environmental sensitivity, and exposed the systems to small radioactive button sources for gamma-rays and neutrons. The small sources did not show obvious real-time signatures in their dynamic resonator output. The second set of tests, performed in the PNNL Radiation and Health Technology Laboratory (PNNL building 318), consisted of gamma-ray and neutron wells where the dose rate could be varied from low to high rates (RHTL 2005). This test allowed assessment of whether the lack of apparent signatures in the previous tests was due to the small amount of radiation.

BUTTON SOURCES AND ENVIRONMENTAL STIMULI

A series of tests were conducted on the GEN-2 (see Figure 3-25) and SRR devices to assess the changes in the resonance as monitored by the RTSA. Various stimuli were used, including light sources and sealed radioactive sources. No obvious effect of the gamma-ray and neutron sources (see Table XIII) could be assessed, so further irradiation testing was performed at higher dose rates (see next section). Sensitivity to vibration (acoustics, microphonics), touch, heat, room lights, lasers, and flashlamps was assessed. See Figure 3-20 for example RTSA waveform captures and Table XIV for a summary of the results.



Figure 3-25: Configuration of the GEN-2 resonator for radiation testing. Si wafer is in the SPDR. The acrylic case shown at right is placed on top of the resonator, and the sources are placed on top of the case.

Table XIII: Button sealed sources used

Isotope	Activity	Activity date	Source #
^{137}Cs	95 μCi	7/11/2011	15272
^{252}Cf	13 μCi	7/11/2011	18360

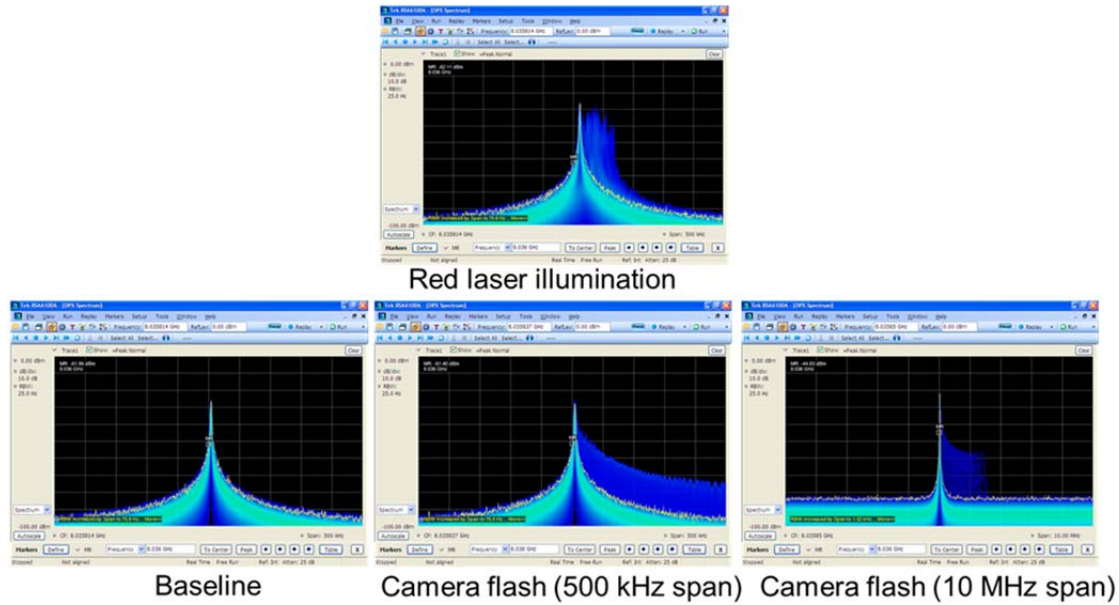


Figure 3-26: Example output waveforms from the RTSA for various stimuli.

Table XIV: Summary of stimulus tests for resonator; an X placed in the γ or n column indicated that they were tested with sealed sources

Sample	Resonator	γ	n	Flash/ laser	Room lights	Human proximity	Magnetic field	Vibration
Si	SPDR	X		Camera flash – high freq large bandwidth; red/green lasers – shift up in freq.	Shift up in freq.	Weak		
LiNbO ₃ -x-cut	SPDR			No change	Shift + 20 kHz, no sidebands	More sensitive than z-cut		
LiNbO ₃ -y-cut	SPDR			No change	No shift visible, not stable, have sidebands	Yes, but resonance never sharpens		
LiNbO ₃ -z-cut	SPDR	X		No change	No shift, sidebands	Yes		
L-Mica#1	SPDR	X	X	No change	No change	Yes		Weak change
Co:YIG	DRR		X	No change	No change	Weak	Weak (AC), strong at close distance	Weak change
CdTe	SRR#1	X	X	Small (but isolated in box)	Shift down in freq.	Weak		Strong change
LiTaO ₃ -PP, unpoled direction	SRR#2			No change	Shift? and strong sidebands	Yes	Shift down in freq	Touch – shift up in freq.
LiTaO ₃ -PP, poled direction	SRR#2	X	X	No change	Shift? and weak sidebands	Yes	Yes	
CdSe	SRR#2							Weak or none
YIG	SRR#2				Sidebands	Yes	Yes	

HIGH DOSE RADIATION

To assess whether the lack of response in the small sealed sources was due to a weak signal and to help ascertain the signature of the radiation itself, a series of high dose rate experiments were performed. In this series of tests, there were new factors to control and understand concerning the effects on the resonators. For instance, we discovered that the fluorescent room lights prevented a very sharp dynamic feedback resonance in the LiNbO₃ and Si samples, but the resonances were still sufficiently sharp to see fine changes due to stray light and other external perturbations.

Other spurious signals were associated with the adjustment of the dose rate. The wells operate by translating a source on an aluminum plate inside a stainless steel tube by a nylon coated stainless steel cable. The wells are approximately 30' deep, and just under the sample surface is a lead plate that moves in and out of the beam depending on the programmed dose rate. The resonators were very sensitive to the movement of the lead plate, but the signature was easy to distinguish. The translation of the source up from the well, however, was more difficult to separate since the stepper motor that switches at 10-20 kHz generated a shift in the LiNbO₃ samples during the final portion of the source placement. A dummy source was not available in this well configuration to allow measurement of analogous effects without the radiation. Other experimental configurations were attempted, such as having the resonator on a PMMA trolley which could be pulled in and out of the radiation beam.

Additionally, the red safety light (seen at the very top of the left picture in Figure 3-20 over the radiation sign), which illuminates when the air monitor reaches a given dose rate, induced carriers in the Si and affected its resonance. Further experiments were performed with the safety light shielded from the resonator. The approximately 20 kHz shifts of the resonance seen with the radiation and red light were still present with the shielded light, but were 10 kHz or less. Thermal drift was assessed with the Co:YIG DRR system, showing ~40 kHz slow total drift over several hours with no source on. Note that even when the source is “off” there is a small dose rate (<0.5 mR/hr) which could be affecting the resonator.

For γ -ray testing, we started with the highest dose rate of 9.9 R/hr (~0.1 Gy/hr). For neutron testing, 100 mR/hr (1 mGy/hr) was used. Since the effects of the radiation were difficult to separate from the environmental variables due to the test configuration, a dose-dependent set of experiments was not conducted. A summary of the results of the samples tested in the wells is shown in Table XV.



Figure 3-27: Gamma-ray well testing with the GEN-2 and SPDR

Table XV: Samples tested with well sources for high dose-rate testing

Sample	Resonator	γ (well#2)	n (well #3)	Room lights	Source translation	Pb plate Vibration	Trolley movement
Si#6	SPDR	X		Room fluorescents spoil Q somewhat; red safety light causes +10 kHz freq shift			
LiNbO ₃ -z-cut	SPDR	X		Spoils Q slightly	Shifts frequency +20 kHz at end		Shift +50 kHz, same with or without radiation
Co:YIG	DRR	X		No change	No change	Transient change, goes away	Some change when sample moves around
LiTaO ₃ -PP, poled direction	SRR#2		X		See transients when source is translating; shifts frequency +20 kHz at end		

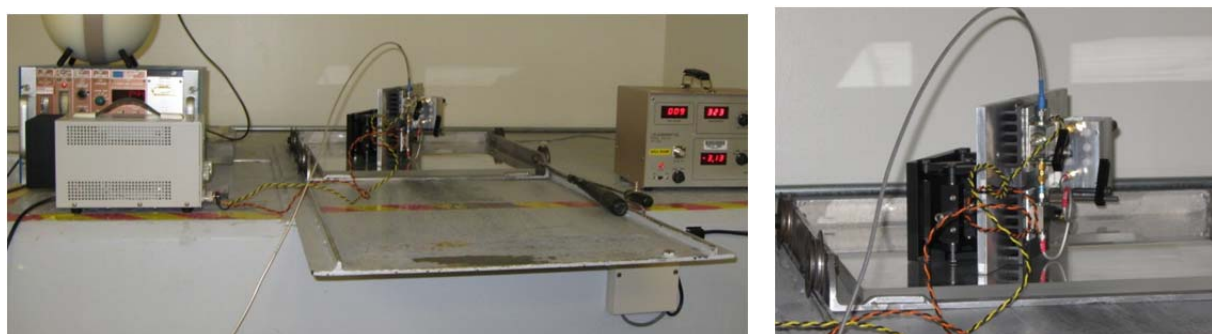


Figure 3-28: Neutron well testing with the SRR#1 and LiTaO₃

4 Conclusions on device feasibility and proposed future work

The original intentions of this project were to discover sensitive electromagnetic materials that would respond to radiation, to study their transient and permanent changes, and to demonstrate a device based on these effects that could be used to remotely monitor radiation exposure. The concept of using alternating current electromagnetic material property changes directly (magnetic permeability, dielectric permittivity, and electrical conductivity) is a novel one distinct from standard methods of using direct current methods to monitor electrical charge or optical photons. This concept provides distinct advantages of being non-contact to the detector material, thus decoupling the sensing and read-out portions of the device.

This project demonstrated materials which permanently change their electromagnetic properties (dielectric permittivity or magnetic permeability) with high doses (~ 1 MGy) of radiation. These experiments did not attempt to find the lower dose threshold level for changes. To investigate lower doses and transient effects, the feedback amplifier in conjunction with various was resonators to create a gain-narrowed regenerative oscillator. It was discovered that the devices are so sensitive that they detect small perturbations in ambient environmental factors such as light, human proximity, and electrical noise. Experiments to assess ionizing radiation effects were compromised by these larger environmentally-induced effects. With follow-on work, the signatures of these environmental factors can be understood and separated from the effects due to episodic low dose ionizing radiation.

This project demonstrated that the non-optimized feedback resonator devices can be used for stand-off detection of their various changes of state due to environmental perturbations. The sharp real-time resonance behavior of the open-face SRR device in Figure 3-26 was measurable from 3 to 4 meters away without antennas on either the receive side (spectrum analyzer) or the resonator side. The maximum stand-off distance was not determined, but based on the signal strength is likely 10's if not 100's of meters. Optimizing an antenna structure on the resonator would be a simple method to utilize these resonator systems as active radio-frequency identification (RFID) tags.

A material sensitive enough to radiation may still be discovered from among the electromagnetic materials, such that radiation-induced changes can be detected using the resonator system. Very fast, sensitive positive feedback circuits of high gain (> 55 dB) and large quality factors (up to 15 million) have been produced order to detect real-time material changes. The bandwidths have not been delimited in order to try to capture the actual shapes of any transient change of the loaded cavities. These efforts are analogous to measuring radiation effects with current amplifiers (I-V) of wide bandwidth, whereas sensitive radiation sensors typically use charge-to-voltage (Q-V) shaping amplifiers with quite narrow band-limited performance. For example, many Q-V pulse shaping preamps create semi-Gaussian transients with ~ 3 microsecond full-width-half-maximum pulses for low count rate sensitive detection. This would correspond to a -3 dB bandwidth of about 160 kHz, whereas in this work, the feedback preamps had wider bandwidths typically > 500 MHz. For example, the Miteq preamp

used with the 287 MHz SRR had a -3 dB bandwidth of 500 MHz, so despite its very good noise figure of 1.3 dB, it would have an output bandwidth disadvantage of square-root (500 E+6/ 160 E+3) or about 55-fold worse input referred noise floor for an optimally coupled Johnson noise level, assuming the same input impedance across the entire band. In fact, the current design does not optimally couple across the full bandwidth of the RF preamp. Until evidence of strong lattice interactions is identified in the detector materials, an optimum band-pass filter window for the regenerative circuits, used to reduce their input-referred noise levels such as is done with commercial FET based Q-V preamps, cannot be determined.

One of the most difficult aspects of this research has been that the feedback amplifiers are sensitive to many controllable and some, as of yet, uncontrollable environmental factors. Many of these have resonator signatures that can easily be distinguished (e.g., Figure 3-26). However, it cannot yet be said for certain what the signature of a radiation event looks like in any particular material in order to optimize the passband features of the preamp. To address this, additional experiments need to be performed.

One possible experiment is a coincidence measurement with the resonator in-line. However, this may be difficult and expensive to perform. Probably first one would want to perform a measurement using a beta source with a chopper wheel which allows knowledge of the “on” and “off” radiation (or alternately a γ source with a tungsten or lead chopper), so the resonator relaxation signals can be identified. This is similar to procedures used in radiosurgery such as “Gammaknife.” Alternatively, shuttered ion beam experiments may be performed. Additionally, the possibility of using a phase-locked loop with the resonators to study fast dynamic error signals without resorting to expensive spectrum analyzers should be explored. This could afford much longer data streaming for potential capture of rare bulk lattice changes, which may be beneficial in identifying fast neutron events.

Finally, some low-temperature resonator experiments should be performed in a dewar to explore the possibility of using the photomagnetic effect in detectors. Currently, the known materials either have Curie temperatures below room temperature or are too electrically conducting to provide good Q for the resonator. It may be, however, that the gains provided by the regenerative feedback will allow use of materials with more loss, such as conductive ferromagnets, since low frequency losses of demagnetized YIG can be overcome by the feedback gains to provide good dynamic Q of 10,000 (Table XI).

A number of different candidate material systems and electromagnetic material change mechanisms have been explored. The key insight from this work is that, for small radioactivities and at room temperature, it is very difficult to perceive small changes in electromagnetic materials in the resonant cavities used here. Part of this involved the relatively small volumes of detector material compared to many conventional radiation detectors. It would be important for future work to design and build cavities where larger volumes of materials could be used. There is a real possibility of identifying new detector materials utilizing changes of magnetic properties, but this short program was not able to identify the best candidate.

Additionally, it would be prudent to test a semiconductor with known γ sensitivity in the feedback resonator (such as CZT at room temperature or Si or Ge at low temperature). Since these materials are known to produce charge carriers and hence conductivity changes with irradiation, they could be used to quantitatively assess the sensitivity of a feedback resonator device. The challenge with CZT is obtaining access to a large enough crystal in the appropriate geometry to operate in the split ring resonator (SRR). One clear piece of follow-on work would be to directly compare shuttered γ -ray or α -particle irradiated CZT conventional detectors with CZT in the SRR. Even though the electromagnetic change mechanism for the resonator with CZT would be just an electrical conductivity change, it would allow the collection of resonator frequency-domain data from a known interaction event. This, then, assists with separating the environmental effects on the detector from the effects due to the radiation source of interest.

5 Programmatic accomplishments

5.1 *Education, collaborations, and team acknowledgements*

This project has supported several undergraduate, graduate, and post-doc students at Tufts University. Additionally, the team had undergraduate summer interns at PNNL who both participated in the DTRA technical review and poster presentation: Brian Walsh summers 2010 and 2011 and Amandeep Chhabra summer 2011. Additionally, the subcontract to Tufts University supported undergraduate and graduate students. The normalized number of students this project supported each calendar year was approximately 1.5.

5.1.1 PNNL team

The following team from PNNL contributed to the success of this project. It is our intention here to acknowledge them (in no particular order):

John S. McCloy, Jim F. Kelly, A. Mark Jones, Doug McMakin, Ron Severtson, Dave Jordan, Brian Riley, Jarrod Crum, S. K. Sundaram, Marvin Warner, Cindy Warner, Tim Droubay, Brian Walsh, Jaehun Chun, Ashu Goel, Chuck Windisch, Amy Qiao, Mark Murphy, Brad Johnson, Weilin Jiang, Ravi Kukkadapu, Wayne Martin, Deena Bean, Pam Kinsey, Teresa Schott, Wendy Bennett, Charlie Bonham, Jonathan Tedeschi, Justin Fernandes, Dave Jordan, Eric Walter

5.1.2 Tufts team

Mohammed Afsar (Professor of Electrical Engineering), Zijing Li (beginning PhD student, 2010), Anjali Sharma (beginning PhD student, 2010-11), Toby Qiu (undergraduate, 2010), Konstantin Korolev (research professor, fall 2009 – winter 2010)

5.1.3 Collaborations

Some related work funded by Department of Energy, National Nuclear Security Administration, Office of Nonproliferation Research & Development (NA-22) in 2009 was performed as a task under a PNNL roadmapping project entitled PL07-SNM-TRM-PD03/Task 6. including a system trade study, commercial resonant cavity purchase, and some GEANT4 modeling for γ ray interaction with some of the proposed detector materials (McCloy et al. 2009).

We have been fortunate enough to have begun a number of informal collaborations as a result of this project. Some of these were one-time contacts and sharing of information, while others have been more prolonged and are likely to continue.

- You Qiang and his graduate students Maninder Kaur and J. Sundarajan, University of Idaho (granular magnetic films)
- Theresa Mayer, Penn State (standoff neutron detection via capacitance)

- Kai Liu and his graduate student Edward Burks, University of California Davis (magnetic modeling)
- Raj Bordia and his graduate student Cliff Leslie, University of Washington (copper manganite spinels)
- Peter Dowben, University of Nebraska Lincoln (periodically poled LiTaO₃)
- Pierre Lucas and his graduate student Ellyn King, University of Arizona (As-S)
- Roman Golovchak, Lviv Scientific Research Institute of Materials, Ukraine &Lehigh University (As-S)
- Kostya Trachenko, Queen Mary College, UK (spin glass theory)
- Aleksey Bolotnikov, Brookhaven National Lab (Cd_{1-x}Mn_xTe crystals)
- Lorraine Sadler, Sandia National Lab (EO neutron detection)

5.2 Technical products

5.2.1 Publications

The following is a summary of publications resulting from this project and collaboration of the investigators on aspects of this project with other organizations. Researchers funded under the DTRA project are underlined in the author list. Several other papers are in revision or are submitted.

1. R. Golovchak, O. Shpotyuk, J. McCloy, B. Riley, C. Windisch, S. K. Sundaram, A. Kovalskiy, H. Jain, "Structural model of homogenous As-S glasses by combined Raman and XPS techniques." *Philosophical Magazine* 90(34): 4489-4501 (2010).
2. R. Golovchak, O. Shpotyuk, A. Kozdras, B. Riley, S. K. Sundaram, J. McCloy, "Radiation effects in physical aging of binary As-(S,Se) glasses." *Journal of Thermal Analysis and Calorimetry*. 103(1):213-218 (2011).
3. J. McCloy, K. Korolev, Z. Li, M. Afsar, S. K. Sundaram, "Millimeter-Wave Dielectric Properties of Single Crystal Ferroelectric and Dielectric Materials." *IEEE Trans. Ultrasonics, Ferroelectrics, and Frequency Control*. 58(1):18-29 (2011).
4. J. A. Sundarajan, D. T. Zhang, Y. Qiang, W. Jiang, J. McCloy, "Helium ion irradiation and magnetic stability of FeO/Fe₃N nanoparticles." *Journal of Applied Physics* 109(7), 07E324-3 (2011)
5. W. Jiang, J. McCloy, A. S. Lea, J. A. Sundarajan, Q. Yau, Y. Qiang. "Magnetization and susceptibility of ion irradiated granular magnetite films," *Physical Review B*. 83(13):134435.
6. P. Lucas, E. A. King, R. G. Erdmann, B. J. Riley, S. K. Sundaram, J. S. McCloy, "Thermal and gamma-ray induced relaxation in As-S glasses: modeling and experiment," *Journal of Physics D: Applied Physics*, 44(39), 395402 (2011).
7. Sundaram, S.K., J. McCloy, B.J. Riley, M.K. Murphy, H.A. Qiao, C.F. Windisch, E.D. Walter, J.V. Crum, R. Golovchak, and O. Shpotyuk, "Gamma Radiation Effects on Physical,

Optical, and Structural Properties of Binary As-S Glasses," *Journal of the American Ceramic Society*, 95(3), 1048-1055 (2012).

8. McCloy, J., R. Kukkadapu, J. Crum, B. Johnson, and T. Droubay, "Size effects on gamma radiation response of magnetic properties of barium hexaferrite powders," *Journal of Applied Physics*, 110(11), 113912-10 (2011).
9. McCloy, J., C. Leslie, T. Kaspar, W. Jiang, and R.K. Bordia, "Magnetic behavior of Ni and Co doped CuMn₂O₄ spinels," *Journal of Applied Physics*, 111(7), 07E149-3 (2012).
10. Korolev, K.A., J. McCloy, and M.N. Afsar, "Ferromagnetic resonance of micro- and nano-sized hexagonal ferrite powders at millimeter waves," *Journal of Applied Physics*, 111(7), 07E113-3 (2012).
11. Chun, J., A. M. Jones, J. McCloy. "Effects of Domain, Grain, and Magnetic Anisotropy Distributions on Magnetic Permeability: Monte-Carlo Approach," *Journal of Applied Physics*. Accepted.

5.2.2 Patents

One US Patent application was filed (February 2012), "Regenerative Feedback Resonant Circuit" with inventors M. Jones, J. Kelly, J. McCloy, and D. McMakin.

5.2.3 Presentations

The following public presentations were made highlighting some of the work performed during the course of this program. Note that this list does not include the DTRA technical reviews (2009, 2010, 2011). Asterisk (*) indicates the presenter.

1. J McCloy,* T Droubay, E Walter, B Riley. "Spin glasses, with emphasis on Cadmium Manganese Telluride." American Ceramic Society Glass & Optical Materials Division meeting, Corning, NY, May 19, 2010.
2. J McCloy.* "Electromagnetic Material Changes for Remote Detection and Monitoring." Radsensing 2010, Argonne, IL, June 8, 2010.
3. W Jiang,* J McCloy, T Droubay, AS Lea, J Sundararajan, Y Qiang. "Irradiation-induced magnetic phase transition in granular magnetite films." (invited) 21st International Conference on the Application of Accelerators in Research and Industry (CAARI) 2010, Ft. Worth, TX, Aug 10, 2010.
4. SK Sundaram,* JS McCloy, MK Murphy, HA Qiao, CF Windisch, Jr., BJ Riley, and BR Walsh. Gamma Radiation Effects on Optical Properties of Binary As-S Glasses (invited). MS&T 2010, Houston, TX, October 20, 2010.
5. W Jiang JS McCloy, AS Lea, JA Sundararajan, Q Yao, and Y Qiang.* "Magnetic phase transition of ion irradiated granular magnetite films." IEEE Intermag: International Magnetics Conference, Taipei, Taiwan, Province Of China, April 28, 2011.

6. S. Sundaram,* B. Riley, A. Qiao, C. Windisch, M. Murphy, J. Crum, J. McCloy, B. Johnson. "New Functionalities in Non-Oxide Glasses." American Ceramic Society Glass and Optical Materials Division, Savannah, GA, May 18, 2011.
7. W Jiang,* JS McCloy, AS Lea, JA Sundararajan, Q Yao, and Y Qiang. 2011. "Ion Irradiation Induced Property Changes in Granular Magnetite Films." (invited), American Ceramic Society Glass and Optical Materials Division, Savannah, GA, May 19, 2011.
8. J. McCloy,* C. Leslie, W. Jiang, B. Johnson, J. Crum, T. Kaspar, G. Exarhos, T. Droubay. "Glassy magnetic behavior in disordered Ni_xCo_{1-x}Mn₂O₄ spinels." (invited), American Ceramic Society Glass and Optical Materials Division, Savannah, GA, May 19, 2011.
9. J. McCloy.* "Novel Radiation Detector Devices and Materials Based on Electromagnetic Property Changes," (invited) Clemson University, Clemson, SC, June 28, 2011.
10. K Korolev, J. McCloy, M. Afsar.* "Transmittance Measurements on Micro- and Nano-sized Ferrite Powders in Millimeter Waves." Poster presentation at 36th International Conference on Infrared, Millimeter, and Terahertz Waves, Houston, TX, October 3, 2011.
11. JS McCloy.* "Effects of Ionizing Radiation on Electromagnetic Materials Relating to Sensing for Nuclear Applications." (invited), speaker at Ohio State University, Nuclear Engineering/ Physics special seminar, Columbus, OH, October 18, 2011.
12. McCloy JS,* CJ Leslie, TC Kaspar, W Jiang, and RK Bordia. 2011. "Magnetic behavior of Ni and Co doped CuMn₂O₄ spinels." 56th annual conference on magnetism and magnetic materials, Scottsdale, AZ, October 31, 2011.
13. Korolev KA,* JS McCloy, and MN Afsar. 2011. "Ferromagnetic Resonance of Micro- and Nano-sized Hexagonal Ferrite Powders at Millimeter Waves." 56th annual conference and magnetism and magnetic materials, Scottsdale, AZ, October 31, 2011.
14. JS McCloy,* W Jiang, CL Warner, and MG Warner. "Measurements and Applications of Magnetic Nanoparticles." (invited), special seminar, Arizona State University, Department of Chemical Engineering, Tempe, AZ, November 2, 2011.
15. Kaur M, JS McCloy, and Y Qiang.* Anomalous Behavior of Hysteresis Loop Caused by Frozen Interface Spins in Core-Shell Iron-Iron Oxide Nanoclusters, Presentation, IEEE Intermag, Vancouver, BC, May 11, 2012.

6 References

Alsen, N. 1925. "Roentgenographische Untersuchungen Der Kristallstrukturen Von Magnetkies, Breithauptit, Pentlandit, Millerit Und Verwandten Verbindungen." *Geologiska Foereningens i Stockholm Foerhandlingar* 47:19-73.

Angadi, B, VM Jali, MT Lagare, VV Bhat, AM Umarji, and R Kumar. 2003a. "Radiation Resistance of Pfn and Pmn-Pt Relaxor Ferroelectrics." *Radiation Measurements* 36(1-6):635-38.

Angadi, B, P Victor, VM Jali, MT Lagare, R Kumar, and SB Krupanidhi. 2003b. "High Energy Li Ion Irradiation Effects in Ferroelectric Pzt and Sbt Thin Films." *Thin Solid Films* 434(1-2):40-48.

Armstrong, EA. 1917. "A Study of Heterodyne Amplification by the Electron Relay." *Proc. of IRE* 5:146-68.

Armstrong, EA. 1914. "Wireless Receiving System." US Patent No. 1,113,149.

ARRL. 1978. *The Radio Amateur's Handbook*. American Radio Relay League (ARRL), Newington, CT.

Arshak, K and O Korostynska, eds. 2006. *Advanced Materials and Techniques for Radiation Dosimetry*. Artech House, Boston.

Arshak, K, O Korostynska, J Harris, D Morris, A Arshak, and E Jafer. 2008. "Properties of Bgo Thin Films under the Influence of Gamma Radiation." *Thin Solid Films* 516(7):1493-98.

Baker-Jarvis, J, MD Janezic, B Riddle, CL Holloway, NG Paulte, and JE Blendell. 2001. "Dielectric and Conductor-Loss Characterization and Measurements on Electronic Packaging Materials." *NIST Technical Note* 1520.

Baltzer, PK, PJ Wojtowicz, M Robbins, and E Lopatin. "Exchange Interactions in Ferromagnetic Chromium Chalcogenide Spinels." *The Physical Review* 151(2):367-77.

Barraclough, KG. 1977. "Crystal Growth of Ferromagnetic Semiconductors." *Progress in Crystal Growth and Characterization* 1:57-84.

Bray, MG, A Kovalev, DH Werner, TS Mayer, and L Takiff. 2008. Chemoselective Salisbury Screen Absorbers for Passive Standoff Detection of Analytes. Presented at *Antennas and Propagation Society International Symposium, AP-S*, 1-4 pp. IEEE,

Bray, MG, AE Kovalev, Z Bayraktar, DH Werner, and TS Mayer. 2007. Reconfigurable Dipole Chaff Elements for Passive Standoff Detection of Chemical Agents. Presented at *Antennas and Propagation Society International Symposium*, 1513-16 pp. IEEE,

Burger, A, K Chattopadhyay, H Chen, J Olivier Ndap, X Ma, S Trivedi, SW Kutcher, R Chen, and RD Rosemeier. 1999. "Crystal Growth, Fabrication and Evaluation of Cadmium Manganese Telluride Gamma Ray Detectors." *Journal of Crystal Growth* 198-199(Part 1):872-76.

Burger, R, S Nuspl, R Spitzer, E Wuori, and F Zieber. 2007. "Radiation Detector Having All-Metal Circuitry Operation of Which Is Based on Electron Spin." US Patent No. 7,220,968.

Carter, CB and MG Norton. 2007. *Ceramic Materials: Science and Engineering*. Springer.

Cetinoneri, B, YA Atesal, RA Kroeger, G Tepper, J Losee, C Hicks, M Rasmussen, and GM Rebeiz. 2010. A Microwave-Based Gamma-Ray Detector. Presented at *Microwave Society IMS*, 469-72 pp. IEEE,

Chao, S and C-C Hung. 1996. "Large Photoinduced Ferroelectric Coercive Field Increase and Photodefined Domain Pattern in Lithium-Tantalate Crystal." *Applied Physics Letters* 69(25):3803-05.

Chen, S, KA Korolev, J Kupershmidt, N Kim, and MN Afsar. 2009. "High-Resolution High-Power Quasi-Optical Free-Space Spectrometer for Dielectric and Magnetic Measurements in Millimeter Waves." *Instrumentation and Measurement, IEEE Transactions on* 58(8):2671-78.

Chizhik, AB, II Davidenko, A Maziewski, and A Stupakiewicz. 1998. "High-Temperature Photomagnetism in Co-Doped Yttrium Iron Garnet Films." *Physical Review B* 57(22):14366.

Chukalkin, YG, VR Shtrits, and BN Goshchitskii. 1983. "Amorphization in Neutron-Irradiated Yttrium Iron Garnet." *Phys. Stat. Sol. (a)* 79:361-66.

Colominas-Broquetas, C, V Van Qui, and EF Bertaut. 1967. "Magnetic Structure of CoCr_2S_4 ." *Bulletin de la Societe Francaise de Mineralogie et de Cristallographie* 90(1):109-10.

Costantini, JM, F Brisard, A Meftah, M Toulemonde, and F Studer. 1995. "Damage of M-Type Baryum Hexaferrites Induced by GeV-Heavy Ion Irradiations." *Nuclear Instruments and Methods in Physics Research Section B: Beam Interactions with Materials and Atoms* 106(1-4):567-72.

Cruickshank, D. 2003. "1-2 Ghz Dielectrics and Ferrites: Overview and Perspectives." *Journal of the European Ceramic Society* 23(14):2721-26.

de Almeida, P, N Franco, JC Soares, and J Räisänen. 2006. "Irradiation-Assisted Photoelastic Domain Wall Formation in X- and Y-Cut Lithium Niobate." *Solid State Communications* 137(6):296-300.

Dobmann, G. 2006. "Nde for Material Characterization of Ageing Due to Thermal Embrittlement, Fatigue and Neutron Degradation." *Int. J. Materials and Product Technology* 26(1/2):122-39.

Edelson, D, RE Jaeger, and JC Williams. 1969. "Transient Effects of Nuclear Radiation on the Dielectric Properties of Refractory Low-Loss Ceramics at Microwave Frequencies." *Journal of the American Ceramic Society* 52(7):359-63.

Enz, U, W Lems, R Metselaar, P Rijnierse, and R Teale. 1969. "Photomagnetic Effects." *Magnetics, IEEE Transactions on* 5(3):467-72.

Enz, U, R Metselaar, and PJ Rijnierse. 1970. "Photomagnetic Effects." *J. Phys. Paris* 32(C1):703-09.

Enz, U and H van der Heide. 1968. "Two New Manifestations of the Photomagnetic Effect." *Solid State Communications* 6(6):347-49.

Fedorov, VA, YA Kesler, and EG Zhukov. 2003. "Magnetic Semiconducting Chalcogenide Spinels: Preparation and Physical Chemistry." *Inorganic Materials* 39(0):S68-S88.

Furdyna, JK. 1988. "Diluted Magnetic Semiconductors." *Journal of Applied Physics* 64(4):R29-R64.

Gibart, P, M Robbins, and JVG Lambrecht. 1973. "New Ferrimagnetic Spinel Compositions in the System $MCr_2S_4-xSe_x$ Where M=Fe, Co, Mn." *Journal of Physics and Chemistry of Solids* 34(8):1363-68.

Golovchak, R, O Shpotyuk, A Kozdras, B Riley, S Sundaram, and J McCloy. 2011. "Radiation Effects in Physical Aging of Binary as-S and as-Se Glasses." *Journal of Thermal Analysis and Calorimetry* 103(1):213-18. 10.1007/s10973-010-0876-8.

Golovchak, R, O Shpotyuk, JS McCloy, BJ Riley, CF Windisch, SK Sundaram, A Kovalskiy, and H Jain. 2010. "Structural Model of Homogeneous as-S Glasses Derived from Raman Spectroscopy and High-Resolution Xps." *Philosophical Magazine* 90(34):4489-501.

Goswami, AK, M Rosenbloom, and RW Teale. 1968. "Microwave Resonance and Magnetic Anneal in Magnesium Ferrous Ferrite." *Journal of Applied Physics* 39(2):828-29.

Harrington, RF. 2001. *Time-Harmonic Electromagnetic Fields*. Ieee Press Series on Electromagnetic Wave Theory, Wiley-Interscience.

Heitmann, H and P Hansen. 1984. "Influence of Annealing on Magnetization, Faraday Rotation, and Optical Absorption of High-Energy Heavy Ion Irradiated Garnet Films." *Magnetics, IEEE Transactions on* 20(5):998-1000.

Hisatake, K. 1977. "Photoinduced Effect on the Permeability of Some Mixed Garnets." *Journal of Applied Physics* 48(7):2971-75.

Hisatake, K, I Matsubara, K Maeda, H Wakao, T Fujihara, Y Kawai, and K Uematsu. 1992. "Gamma-Ray-Induced Disaccommodation of Permeability in Single Crystal of Yttrium Aluminum Garnet." *Journal of Magnetism and Magnetic Materials* 112:387-88.

Hisatake, K and T Matsuyama. 1974. "Photoinduced Decrease of Permeability in Gd_{1-x}Pb_x." *Japanese Journal of Applied Physics* 13(12):2061-62.

Hisatake, K, K Ohta, N Ichinose, and H Yokoyama. 1974. "X-Ray Induced Decrease of Permeability in Y_{1-x}Gd_x Single Crystals with Pb Impurity." *Physica Status Solidi (a)* 26(1):K79-K82.

Ishihara, O, T Mori, H Sawano, and M Nakatani. 1980. "A Highly Stabilized Gaas Fet Oscillator Using a Dielectric Resonator Feedback Circuit in 9-14 Ghz." *IEEE Trans. MTT* 28(8):817-24.

Jellinek, F. 1957. "The Structures of the Chromium Sulphides." *Acta Crystallographica* 10:620-28.

Jentjens, L, K Peithmann, K Maier, H Steigerwald, and T Jungk. 2009. "Radiation-Damage-Assisted Ferroelectric Domain Structuring in Magnesium-Doped Lithium Niobate." *Applied Physics B: Lasers and Optics* 95(3):441-45.

Jiang, W, JS McCloy, AS Lea, JA Sundararajan, Q Yao, and Y Qiang. 2011. "Magnetization and Susceptibility of Ion-Irradiated Granular Magnetite Films." *Physical Review B* 83(13):134435.

Jin, Y, R Xu, J Quan, Z Wang, Q Meng, Y Sun, F Ma, J Han, G Liu, J Liu, and C Li. 1996. "1 GeV Ar Ions Induced Amorphization in Garnet." *Nuclear Instruments and Methods in Physics Research Section B: Beam Interactions with Materials and Atoms* 107(1-4):227-31.

Jonker, HD. 1974. "Photomagnetic Effects in Single-Crystal Ru-Doped Lithium Ferrite." *Journal of Solid State Chemistry* 10(2):116-21.

Kalinnikov, VT, TG Aminov, and VM Novotortsev. 2003. "Physical Chemistry of the Magnetic Semiconductor Cdcr₂se4." *Inorganic Materials* 39(10):997-1012.

Kawai, H and T Sato. 1999. "Magnetic Response of Cd_{0.63}Mn_{0.37}Te under Illumination: Dynamic Behavior of Spin Glass with Step-Like Heating and Cooling." *Journal of Applied Physics* 85(10):7310-15.

Kelly, JF and A Gallagher. 1987. "Efficient Electro-Optic Modulator for Optical Pumping of Na Beams." *Review of Scientific Instruments* 58(4):563-66.

Kim, S-S, Y-C Yoon, and K-H Kim. 2003. "Electromagnetic Wave Absorbing Properties of High-Permittivity Ferroelectrics Coated with Ito Thin Films of 377 Ohm." *Journal of Electroceramics* 10:95-101.

Korolev, KA, JS McCloy, and MN Afsar. 2012. "Ferromagnetic Resonance of Micro- and Nano-Sized Hexagonal Ferrite Powders at Millimeter Waves." *Journal of Applied Physics* 111(7):07E113-3.

Krupka, J and RG Geyer. 1996. "Complex Permeability of Demagnetized Microwave Ferrites near and above Gyromagnetic Resonance." *IEEE Trans. Magnetics* 32(3):1924-33.

Kumara, LSR, M Hidaka, N Tokiwa, J Awaka, T Hagino, S Nagata, and YJ Park. 2008. "Correlation between Structural and Magnetic Properties of Half-Metallic Spinel Cu₂S₄ Due to the Order-Disorder Transition of 3d²(T_{2g}) Orbitals of V³⁺ Ions." *physica status solidi (b)* 245(11):2539-49.

Lacklison, DE, J Chadwick, and JL Page. 1971. "Photomagnetic Effect in Ferric Borate." *Journal of Applied Physics* 42(4):1445-46.

Lems, W, R Metselaar, PJ Rijnierse, and U Enz. 1970. "Light-Induced Increase in Domain-Wall Stiffness in Si-Doped Yig." *Journal of Applied Physics* 41(3):1248-49.

Lems, W, PJ Rijnierse, PF Bongers, and U Enz. 1968. "Photomagnetic Effect in a Chalcogenide Spinel." *Physical Review Letters* 21(24):1643-45.

Lucas, P, EA King, RG Edermann, BJ Riley, SK Sundaram, and JS McCloy. 2011. "Thermal and Gamma-Ray Induced Relaxation in as-S Glasses: Modelling and Experiment." *Journal of Physics D: Applied Physics* 44(39):395402.

Marais, A and T Merceron. 1974. "Electronic Hopping and Photomagnetic Effect in Several Ferrimagnetic Spinels." *Phys. Stat. Sol. (a)* 22:K209-K13.

Mayer, T. 2010. "Reflective Radiation Sensitive Surface." June, 2010,

McCloy, J, R Kukkadapu, J Crum, B Johnson, and T Droubay. 2011a. "Size Effects on Gamma Radiation Response of Magnetic Properties of Barium Hexaferrite Powders." *Journal of Applied Physics* 110(11):113912-10. 10.1063/1.3665769.

McCloy, JS, D Jordan, JF Kelly, DL McMakin, BR Johnson, and LW Campbell. 2009. *Electromagnetic Material Changes for Remote Detection and Monitoring: A Feasibility Study: Progress Report*. Report No. PNNL-18863, Pacific Northwest National Laboratory, Richland, Washington.

McCloy, JS, KA Korolev, Z Li, M Afsar, and SK Sundaram. 2011b. "Millimeter-Wave Dielectric Properties of Single Crystal Ferroelectric and Dielectric Materials." *IEEE Transactions on Ultrasonics, Ferroelectrics, and Frequency Control* 58(1):18-29.

McCloy, JS, C Leslie, T Kaspar, W Jiang, and RK Bordia. 2012. "Magnetic Behavior of Ni and Co Doped Cu₂O₄ Spinels." *Journal of Applied Physics* 111(7):07E149-3.

McCloy, JS, BJ Riley, SK Sundaram, HA Qiao, JV Crum, and BR Johnson. 2010. "Structure-Optical Property Correlations of Arsenic Sulfide Glasses in Visible, Infrared, and Sub-Millimeter Regions." *Journal of Non-Crystalline Solids* 356(25-27):1288-93.

Meillon, S, F Studer, M Hervieu, and H Pascard. 1996. "Changes in Magnetic Properties of Magnetite Fe₃O₄ Ceramics Induced by High Energy Heavy Ion Irradiation." *Nuclear Instruments and Methods in Physics Research Section B: Beam Interactions with Materials and Atoms* 107(1-4):363-67.

Metselaar, R and MAH Huyberts. 1974. "Influence of Dopants on Photomagnetic Effects in Yig." *Philips Research Reports* 29:453-75.

Metselaar, R and MAH Huyberts. 1973. "The Stoichiometry and Defect Structure of Yttrium Iron Garnet and the Nature of the Centres Active in the Photomagnetic Effect." *Journal of Physics and Chemistry of Solids* 34(12):2257-63.

Metselaar, R, MAH Huyberts, and H Logmans. 1975. "Light-Induced Changes in Permeability of N- and P-Type Yig Films." *Journal of Applied Physics* 46(7):3171-74.

Mosiniewicz-Szablewska, E and H Szymczak. 1993. "Photomagnetic Effect in the CdCr₂Se₄ Ferromagnetic Semiconductor." *Physical Review B* 47(14):8700.

Mousa, MA, AM Summan, MA Ahmed, and AM Badawy. 1989. "Electrical Conduction in G-Irradiated and Unirradiated Fe₃O₄, CdFe₂O₄ and Co_xZn_{1-x}Fe₂O₄ (0 < X < 1) Ferrites." *Journal of Materials Science* 24:2478-82.

Nagaev, EL. 1988. "Photoinduced Magnetism and Conduction Electrons in Magnetic Semiconductors." *Phys. Stat. Sol. (a)* 145:11-64.

Naidu, SM. 2011. *Engineering Physics-I*. Pearson Education India.

Nolulyak, ES, MA Plotkin, EG Zhukov, VI Nefedov, and VA Fedorov. 1987. "Preparation, Composition, and Properties of CoCr₂S₄ Single Crystals." *Inorganic Materials* 23(8):1229-31.

Ogasawara, T, K Ohgushi, Y Tomioka, KS Takahashi, H Okamoto, M Kawasaki, and Y Tokura. 2005. "General Features of Photoinduced Spin Dynamics in Ferromagnetic and Ferrimagnetic Compounds." *Physical Review Letters* 94(8):087202.

Ohgushi, K, Y Okimoto, T Ogasawara, S Miyasaka, and Y Tokura. 2008. "Magnetic, Optical, and Magneto-optical Properties of Spinel-Type A_aCr₂X₄ (a = Mn, Fe, Co, Zn, Cd; X = O, S, Se)." *Journal of the Physical Society of Japan* 77(3):034713-1 - 13-16.

Okimoto, Y, Y Ogimoto, M Matsubara, Y Tomioka, T Kageyama, T Hasegawa, H Koinuma, M Kawasaki, and Y Tokura. 2002. "Direct Observation of Photoinduced Magnetization in a Relaxor Ferromagnet." *Applied Physics Letters* 80(6):1031-33.

Parkhomenko, VD, SF Dubinin, BN Goshchitskii, YG Chukalkin, SK Sidorov, VG Vologin, and VV Petrov. 1976. "Peculiarities of Radiation Damage in Ferrites with Spinel Structure." *Physica Status Solidi A* 38:57-66.

Parkin, J, PJ Sellin, AW Davies, A Lohstroh, ME Özsan, and P Seller. 2007. "A Particle Response of Undoped Cd_{1-x}Sn_xO₄." *Nuclear Instruments and Methods in Physics Research Section A: Accelerators, Spectrometers, Detectors and Associated Equipment* 573(1-2):220-23.

Podsekin, AK and BD Zaitsev. 1982. "Relationship between the Saturation Magnetization and the Curie Temperature of Yttrium Iron Garnet." *Sov. Phys. Solid State* 24(2):342-43.

Podsekin, AK, BD Zaitsev, and II Kuz'min. 1982. "Effects of Neutron Radiation from a Reactor on the Magnetic Spectrum Saturation Magnetization of Yttrium Ferrogarnet." *Sov. Phys. Tech. Phys.* 27(1):54-56.

Pozar, DM. 2005. *Microwave Engineering*. 3rd ed. ed., John Wiley & Sons, Hoboken, NJ.

RHTL. 2005. *Radiation and Health Technology Laboratory Capabilities*. Report No. PNNL-10354, Rev 2, Pacific Northwest National Laboratory, Richland, WA.

Riedel, E and E Horváth. 1969. "Spinelle Mit Substituierten Nichtmetallteilgittern. I. Röntgenographische Und Ir-Spektroskopische Untersuchung Der Systeme ZnCr₂(S_{1-x}Se_x)₄, CdCr₂(S_{1-x}Se_x)₄ Und ZnCr₂(Se_{1-x}Te_x)₄." *Zeitschrift für anorganische und allgemeine Chemie* 371(5-6):248-55.

Robbins, M, PK Baltzer, and E Lopatin. 1968. "Ferromagnetic Halo-Chalcogenide Spinels (CuCr₂X₃Y) and Some Properties of the Systems CuCr₂Se₃Br-CuCr₂Se₄ and CuCr₂Te₃I-CuCr₂Te₄." *Journal of Applied Physics* 39(2):662-64.

Roberts, AP, CR Pike, and KL Verschueren. 2000. "First-Order Reversal Curve Diagrams: A New Tool for Characterizing the Magnetic Properties of Natural Samples." *Journal of Geophysical Research* 105(N12):28,461-28,75.

Roy, R and A Pandya. 2005. "Evaluation of Gamma and Neutron Irradiation Effects on the Properties of Mica Film Capacitors." *Bull. Mater. Sci.* 28(7):719-24.

Seki, M, AKM Akther Hossain, H Tabata, and T Kawai. 2005a. "Photocontrol of Magnetization in Al-Substituted Fe₃O₄ Thin Films." *Solid State Communications* 133(12):791-96. 10.1016/j.ssc.2004.12.048.

Seki, M, AKM Hossain, T Kawai, and H Tabata. 2005b. "High-Temperature Cluster Glass State and Photomagnetism in Zn- and Ti-Substituted NiFe₂O₄ Films." *Journal of Applied Physics* 97(8):083541-6.

Sleight, AW and HS Jarrett. 1968. "Preparation and Properties of Some Copper Chromium Halochalcogenides with the Spinel Structure." *Journal of Physics and Chemistry of Solids* 29(5):868-70.

Smit, J and HPJ Wijn. 1959. *Ferrites: Physical Properties of Ferrimagnetic Oxides in Relation to Their Technical Applications*. Wiley Series on the Science and Technology of Materials, John Wiley & Sons, New York.

Smith, M, A Dissanayake, and HX Jiang. 1994. "Relaxation of Spin-Glass Magnetization in $Cd_{1-x}Mn_xTe$ Diluted Magnetic Semiconductors." *Physical Review B* 49(7):4514.

Srikanth, H, MH Phan, MB Morales, CN Chinnasamy, B Latha, and VG Harris. 2009. "Magnetocaloric Effect in Bulk and Nanostructured $Gd(3)Fe(5)O(12)$ Materials." *Journal of Physics D-Applied Physics* 42(11). 10.1088/0022-3727/42/11/115007.

Sternberg, AR, A Krumins, K Kundzins, V Zauls, I Aulika, L Cakare, R Bittner, H Weber, K Humer, D Lesnyh, D Kulikov, and Y Trushin. 2003. Irradiation Effects in Lead Zirconate Thin Films. In *Proceedings of Advanced Organic and Inorganic Optical Materials*, 341-47 pp. SPIE

Sternberg, AR, A Spule, L Shebanov, E Birks, P Kulis, HW Weber, FM Sauerzopf, H Klima, and U Ulmanis. 1997. Radiation Effects in Transparent Ferroelectric Ceramics. In *Proceedings of Optical Inorganic Dielectric Materials and Devices*, 186-92 pp. SPIE,

Stevenson, AW and Z Barnea. 1984. "Anharmonic Thermal Vibrations and the Position Parameter in Wurtzite Structures. II. Cadmium Selenide." *Acta Crystallographica* B40:530-37.

Studer, F, C Houpert, D Groult, JY Fan, A Meftah, and M Toulemonde. 1993. "Spontaneous Magnetization Induced in the Spinel $ZnFe_2O_4$ by Heavy Ion Irradiation in the Electronic Stopping Power Regime." *Nuclear Instruments and Methods in Physics Research Section B: Beam Interactions with Materials and Atoms* 82(1):91-102.

Stupakiewicz, A, A Maziewski, I Davidenko, and V Zablotskii. 2001. "Light-Induced Magnetic Anisotropy in Co-Doped Garnet Films." *Physical Review B* 64(6):064405.

Sundaram, SK, JS McCloy, BJ Riley, MK Murphy, HA Qiao, CF Windisch, ED Walter, JV Crum, R Golovchak, and O Shpotyuk. 2012. "Gamma Radiation Effects on Physical, Optical, and Structural Properties of Binary as-S Glasses." *Journal of the American Ceramic Society* 95(3):1048-55. 10.1111/j.1551-2916.2011.04938.x.

Sundararajan, JA, DT Zhang, Y Qiang, W Jiang, and JS McCloy. 2011. "Magnetic Stability of He^+ Ion Irradiated $FeO + Fe_3N$ Granular Films." *Journal of Applied Physics* 109(7):07E324-3. 10.1063/1.3560119.

Taber, RC and CA Flory. 1995. "Microwave Oscillators Incorporating Cryogenic Sapphire Dielectric Resonators." *IEEE Trans. Ultrasonics, Ferroelectrics, and Frequency Control* 42(1):111-19.

Teale, RW and DW Temple. 1967a. "Photomagnetic Anneal a New Magneto-Optic Effect in Si-Doped Yttrium Iron Garnet." *Physical Review Letters* 19(16):904-&.

Teale, RW and DW Temple. 1967b. "Photomagnetic Anneal, a New Magneto-Optic Effect, in Si-Doped Yttrium Iron Garnet." *Physical Review Letters* 19(16):904.

Teale, RW, DW Temple, U Enz, and RF Pearson. 1969. "Infrared Sensitive Ferrimagnetics." *Journal of Applied Physics* 40(3):1435-41.

Teale, RW, DW Temple, and DI Weatherley. 1970. "Magnetic Anisotropy and Magnetic Anneal in Silicon-Doped Yttrium Iron Garnet." *Journal of Physics C: Solid State Physics* 3(6):1376-87.

Teale, RW and DI Weatherley. 1973. "Photoinduced Changes in the Magnetic Anisotropy of Silicon-Doped Yttrium Iron Garnet." *J. Phys. C: Solid State Phys.* 6:750-54.

Tepper, G and J Losee. 2001. "A Contactless, Microwave-Based Radiation Detector." *Nuclear Instruments and Methods in Physics Research Section A: Accelerators, Spectrometers, Detectors and Associated Equipment* 458:472-77.

Tepper, G and J Losee. 1997. "Detection of Single Photon Ionization Events Using a Contactless Microwave Technique." *Review of Scientific Instruments* 68(1):55-57.

Toulemonde, M, G Fuchs, N Nguyen, F Studer, and D Groult. 1987. "Damage Processes and Magnetic Field Orientation in Ferrimagnetic Oxides $Y_3Fe_5O_{12}$ and $BaFe_{12}O_{19}$ Irradiated by High-Energy Heavy Ions: A Mossbauer Study." *Physical Review B* 35(13):6560.

Ubizskii, SB, AO Matkovsky, RM Kholyavka, and MM Rak. 1993. "Investigation of Radiation-Stimulated Processes in Epitaxial Yttrium-Iron Garnet Films." *Journal of Magnetism and Magnetic Materials* 125(1-2):110-12.

Ubizskii, SB, AO Matkovskii, and M Kuzma. 1996. "Irradiation-Induced Effects in Yttrium-Iron Garnet Films." *Journal of Magnetism and Magnetic Materials* 157-158:279-80.

Valenzeula, R. 1994. *Magnetic Ceramics*. Chemistry of Solid State Materials, Cambridge University Press, Cambridge, UK.

Wehmeier, FH, ET Keve, and SC Abrahams. 1970. "Preparation, Structure, and Properties of Some Chromium Selenides. Crystal Growth with Selenium Vapor as a Novel Transport Agent." *Inorganic Chemistry* 9(9):2125-31.

Wojtowicz, PJ. 1969. "Semiconducting Ferromagnetic Spinels." *IEEE Transactions on Magnetics* 5(4):840-48.

Wurlitzer, M. 1981. "A Model of the Photomagnetic Effect in $Y_{1-x}Fe_xSi$." *Phys. Stat. Sol. (a)* 64:539-47.

Young, JL, RO Nelson, and JF Kelly. 2003. "Radio Frequency Characterization of a Split-Ringed, Electrically Small Electro-Optical Bulk Modulator." *Review of Scientific Instruments* 74(10):4529-35.

Zamani-Meymian, M-R, L Jentjens, N Raeth, K Peithmann, and K Maier. 2010. "Thermal and Long-Term Stability of Fast-Ion-Irradiation-Induced Refractive Index Changes in Lithium Niobate Crystals." *Applied Physics A: Materials Science & Processing* 98(4):909-12.

DISTRIBUTION LIST
DTRA-TR-15-45

DEPARTMENT OF DEFENSE

DEFENSE THREAT REDUCTION
AGENCY
8725 JOHN J. KINGMAN ROAD
STOP 6201
FORT BELVOIR, VA 22060
ATTN: D. PETERSEN

DEFENSE TECHNICAL
INFORMATION CENTER
8725 JOHN J. KINGMAN ROAD,
SUITE 0944
FT. BELVOIR, VA 22060-6201
ATTN: DTIC/OCA

**DEPARTMENT OF DEFENSE
CONTRACTORS**

QUANTERION SOLUTIONS, INC.
1680 TEXAS STREET, SE
KIRTLAND AFB, NM 87117-5669
ATTN: DTRIAC